

The kinematics and spatial distribution of stellar populations in E+A galaxies

Michael B. Pracy^{1*}, Harald Kuntschner², Warrick J. Couch³, Chris Blake³, Kenji Bekki⁴ and Frank Briggs¹

¹*Research School of Astronomy & Astrophysics, The Australian National University, Weston Creek, ACT 2611, Australia*

²*Space Telescope European Coordinating Facility, European Southern Observatory, Karl-Schwarzschild Strasse 2, 85748, Garching, Germany*

³*Centre for Astrophysics and Supercomputing, Swinburne University of Technology, P.O. Box 218, Hawthorn, VIC, 3122, Australia*

⁴*School of Physics, University of New South Wales, Sydney NSW 2052, Australia*

Received 0000; Accepted 0000

ABSTRACT

We have used the GMOS instrument on the 8.1-m Gemini–South telescope to obtain spatially–resolved two–colour imaging and integral field unit (IFU) spectroscopy of a sample of ten nearby ($z = 0.04$ – 0.20) “E+A” galaxies selected from the Two Degree Field Galaxy Redshift Survey. These galaxies have been selected to lie in a variety of environments from isolated systems to rich clusters. Surface brightness profiles measured using our imaging data show the isophotal profiles of our sample are generally $r^{1/4}$ –like, consistent with a sample dominated by early–type galaxies. Only one galaxy in our sample has an obvious exponential (‘disk–like’) component in the isophotal profile. This is further underscored by all galaxies having early Hubble type morphological classifications, and showing a behaviour in the central velocity dispersion–absolute magnitude plane that is consistent with the Faber–Jackson relation, once the transitory brightening that occurs in the E+A phase is corrected for. In addition, two-thirds of our sample shows clear evidence of either ongoing or recent tidal interactions/mergers, as evidenced by the presence of tidal tails and disturbed morphologies. While all the galaxies in our sample have total integrated colours that are relatively blue (in keeping with their E+A status), they show a diversity of colour gradients, possessing central core regions that are either redder, bluer, or indistinct in colour relative to their outer regions. The E+A spectra are well fitted by that of a young stellar population, the light from which is so dominant that it is impossible to quantify the presence of the underlying old stellar population. Consistent with other recent findings, there is little evidence for radial gradients in the Balmer absorption line equivalent widths over the central few kiloparsecs (< 4 kpc), although we are unable to search for the previously reported radial gradients at larger galacto–centric radii due to the limited spatial extent of our IFU data. Kinematically, the most striking property is the significant and unambiguous rotation that is seen in all our E+A galaxies, with it being generally aligned close to the photometric major axis. This is contrary to the findings of Norton et al. (2001), who found little or no evidence for rotation in a very similar sample of nearby E+A galaxies. We also clearly demonstrate that our E+A galaxies are, in all but one case, consistent with being “fast rotators” (Emsellem et al. 2007), based on their internal angular momentum per unit mass measured as a function of radius and ellipticity. We argue that the combination of disturbed morphologies and significant rotation in these galaxies supports their production via gas–rich galaxy mergers and interactions. The large fraction of fast rotators argues against equal mass mergers being the dominant progenitor to the E+A population.

Key words: galaxies: evolution – galaxies: formation – galaxies: stellar content

1 INTRODUCTION

Galaxy mergers and interactions are a fundamental driving

* E-mail: mpracy@mso.anu.edu.au

this picture. They are conspicuous by their unusual spectra (Dressler & Gunn 1983): strong hydrogen Balmer absorption lines (implying a relatively young ‘A’-type stellar population) superimposed upon an elliptical (‘E’) galaxy spectrum with no optical emission lines (implying no ongoing star formation). The A-stars must have been produced by a powerful recent episode of star formation, which has been suddenly truncated in the past 1 Gyr (Couch & Sharples 1987; Poggianti et al. 1999). The spectroscopic data are also consistent with the uniform truncation of star formation in a disk, without necessarily requiring a starburst (e.g. Shioya et al. 2004). Observational evidence indicates that the E+A phenomenon may, in part, mark the transitory phase between star-forming disk galaxies and quiescent spheroidal systems (e.g. Caldwell et al. 1996; Zabludoff et al. 1996; Norton et al. 2001, hereafter NGZZ).

Understanding the origin of the E+A phase is complicated by the fact that E+A galaxies inhabit a wide range of environments, in a manner that depends upon both redshift and luminosity. In summary: luminous E+A galaxies are commonplace in intermediate redshift clusters, where they were first identified and studied (Dressler & Gunn 1983). In the low-redshift universe cluster E+A’s are still frequent, but their luminosities are much lower than their higher-*z* counterparts (Poggianti et al. 2004). Most luminous E+A galaxies at low redshift are located in the field, although they represent a very low fraction of the overall field galaxy population (Zabludoff et al. 1996).

The physical mechanism(s) responsible in triggering intense star-formation and subsequently rapidly quenching it remains the key question to better understand the E+A galaxy phase and the role it plays in galaxy evolution. There have been several mechanisms suggested which could give rise to the E+A spectral signature. These include major mergers (Mihos & Hernquist 1996; Bekki et al. 2005), unequal mass mergers (Bekki et al. 2001) and galaxy interactions (Bekki et al. 2005). For E+As galaxies residing in clusters, other plausible mechanisms exist, such as: interaction with the strongly varying global cluster tidal field (Bekki 1999), galaxy harassment (Moore et al. 1998) or interaction with the hot intra-cluster gas (Gunn & Gott 1972; Dressler & Gunn 1983; Bothun & Dressler 1986).

The continuous accretion of cold gas onto galaxies is predicted in galaxy formation models (e.g. Birnboim & Dekel 2003; Kereš et al. 2005; Semelin & Combes 2005; Dekel & Birnboim 2006) and could also be a driver of galaxy evolution. Such a mechanism, however, should not induce a starburst, but rather contribute to slow and continuous levels of star formation. Given the large and rapid changes needed to produce the spectral properties of E+A galaxies, and the evidence that a high fraction of these systems are morphologically disturbed, accretion of cold gas from large scale structure is unlikely to be an important mechanism in E+A formation.

There is evidence that the E+As in the low-redshift field are the result of merging or tidal interactions between galaxies. Ground-based imaging of a sample of 21 E+A galaxies drawn from the Las Campanas Redshift Survey (LCRS) revealed an increased incidence of tidal features associated with these galaxies implying galaxy interactions or galaxy mergers had taken place (Zabludoff et al. 1996). Their conclusions were later confirmed using high resolution Hubble

Space Telescope imaging of the LCRS sample (Yang et al. 2008), which found a high incidence of tidal features consistent with mergers or interactions. Samples of E+A galaxies constructed from larger redshift surveys reinforce these ideas. Using a robust sample of E+A galaxies selected from the Two Degree Field Galaxy Redshift Survey (2dFGRS; Colless et al. 2001), Blake et al. (2004) concluded that their sample was consistent with a major merger origin based on their morphologies, incidence of tidal disruption, and luminosity function. In addition, Goto’s (2005) study of a sample of low-redshift E+A galaxies selected from the Sloan Digital Sky Survey (SDSS; Abazajian et al. 2004) revealed an excess in the projected galaxy density on small scales surrounding the E+A galaxies providing a strong hint of galaxy-galaxy interactions as a formation mechanism.

A more powerful and direct method of inferring the physical mechanism(s) responsible for the E+A galaxy phase is to study the internal properties of individual galaxies. The kinematics and spatial distribution of the stellar populations of a galaxy in the E+A phase holds a wealth of information about the history of its formation and is critical information for discerning which of the candidate mechanisms is responsible. Mergers and tidal interaction are expected to give rise to star formation which is centrally concentrated as gas is funneled to the galactic center (Noguchi 1988; Barnes & Hernquist 1991; Mihos et al. 1992; Mihos & Hernquist 1996; Bekki et al. 2005; Hopkins et al. 2009). For an equal mass merger (e.g. two massive spirals), the remnant should settle quickly to the virial plane and be dynamically pressure supported (NGZZ; Bekki et al. 2005). Such mergers can also produce rotating remnants a small fraction of the time, but this requires specific merger configurations (Bekki et al. 2005; Bournaud et al. 2008). In the case of unequal mass mergers and tidal interactions, rotation of the young stellar populations is generally expected (Bekki et al. 2005). In contrast, if star formation is simply truncated abruptly in a ‘normal’ star-forming disk, the young stellar population should be spread throughout the extent of the galaxy and rotation should be present in both the young and old stellar populations (NGZZ; Bekki et al. 2005; Pracy et al. 2005).

Spatially resolved spectroscopic studies of E+A galaxies residing in clusters have revealed a young stellar population which is widely spread throughout the galaxy and not confined to the galaxy core; observations have also shown evidence for strong rotation in these galaxies (Caldwell et al. 1996; Franx 1993). Pracy et al. (2005) found diversity in the spatial distribution of the young population in the E+A galaxy population in the intermediate redshift cluster AC114; some E+As have a centrally concentrated young stellar population consistent with a tidal or merger origin and others revealed a more distributed young star component consistent with the truncation of a spiral disk. The small number of examples of spatially resolved spectroscopy of E+A galaxies in the nearby field have generally revealed a central concentration of the young stellar population (NGZZ; Goto et al. 2008) although there exist exceptions (Swinbank et al. 2005). NGZZ used long slit spectroscopy to study the internal kinematics of field E+A galaxies over the central $\sim 2\text{--}4$ kpc. They found little difference in the kinematics of the young and old stellar populations and that in all but a small fraction of cases the E+As showed little or no rotation. They interpret their results as being con-

sistent with E+As being in the midst of a transformation from gas rich, rotationally supported disks into gas poor, pressure supported early-type galaxies. Yamauchi & Goto's (2005) investigation of the two-dimensional color distributions of E+A galaxies found an excess of galaxies with blue cores (relative to normal early-type galaxies) and they interpreted their results as being consistent with the galaxies having undergone a centralized star-burst caused by a merger or interaction. Yang et al. (2008), using HST imaging found diversity in the internal color distributions of the LCRS sample, but also found a tendency toward bluer centres which they interpreted as evidence for merger/interaction-induced star formation.

In this paper we present high quality imaging and spatially-resolved two-dimensional spectroscopy of a sample of robustly selected E+A galaxies from the 2dFGRS (Blake et al. 2004). These observations consist of deep two color imaging with GMOS on the 8.1-m Gemini South Telescope to investigate internal color gradients and to look for faint tidal tails or disturbances which could be symptomatic of a recent interaction or merger. We have also obtained Integral Field Unit (IFU) observations with GMOS in order to study the internal kinematics and line-strength distribution. Throughout we adopt an $\Omega_M = 0.3, \Omega_\Lambda = 0.7$ and $H_0 = 70 \text{ kms}^{-1}\text{Mpc}^{-1}$ cosmology.

2 OBSERVATIONS AND DATA REDUCTION

2.1 Sample

We have selected 10 relatively bright ($b_J \sim 18.4$) and nearby ($z < 0.2$) E+A galaxies from the 2dFGRS E+A catalogue compiled by Blake et al. (2004) for follow up with high resolution imaging and spatially resolved spectroscopic observations. The selection criteria used for the Blake et al. (2004) sample was based on that of Zabludoff et al. (1996), specifically a galaxy was required to have [OII] equivalent width of less than 2.5 \AA in emission and a mean Balmer absorption line strength (based on a weighted combination of the $H\delta$, $H\gamma$ and $H\beta$ lines) of greater than 5.5 \AA in absorption. These galaxies have already had their morphologies and external environments investigated by Blake et al. (2004) and we have selected our sample to span a wide range of environments. Specifically, four galaxies are 'isolated', four are located in groups (i.e. linked to other survey objects by a percolation algorithm, Eke et al. 2004) and two galaxies inhabit cluster environments. The details of our target galaxies are summarized in Table 1.

2.2 Imaging

2.2.1 Observations

For each galaxy in our sample we obtained g - and r -band imaging using GMOS on Gemini-South. The imaging was obtained in queue mode between 2005 September 1 and 2005 December 4. The imaging consisted of $3 \times 420.5 \text{ s}$ exposures for each object, in each band, giving a total integration time of 1261.5 s . Longer integrations were obtained for E+A.4 and E+A.5. The details of the imaging observations are given in Table 2. The imaging was taken in seeing of $\sim 1''$ and never worse than $1.2''$, and was sampled with

$0.145''$ pixels (see Table 2). The final reduced g -band images of each target are shown in the first column of Figure 1.

2.2.2 Data reduction

The imaging was reduced in the standard manner using the IRAF Gemini package task GIREDUCE to perform bias and flat field corrections and remove the overscan region. The individual exposures were then combined using the task GEMCOMBINE. Since no standard star calibrations were obtained, photometric zero points were calculated by matching stars in the field to the SuperCosmos catalogue. The SuperCosmos magnitudes were converted from b_J and r_F to g and r using the filter conversions given in Cross et al. (2004) and references therein. For each GMOS observation we had between four and ten stars that were suitable for use in calibration (isolated within a suitable magnitude range). It is known that a small fraction of objects in the SuperCosmos catalogue have spurious magnitudes with errors of order $\sim 0.5 \text{ mags}$. We therefore excluded the few obvious outliers in calculating the zero-point values. The rms scatter in the derived zero point for all images was $\sim 0.05 \text{ mags}$. This calibration is more than adequate for our purposes since the most important information is contained in the relative colour differences across individual objects rather than their absolute colours.

The point spread function (PSF) for each image was measured from stars near to the target galaxy and modelled as an elliptical Gaussian (since the delivered images can have a slight asymmetry). We created colour images by carefully aligning the g - and r -band images and matching the PSFs by convolving each image with an elliptical Gaussian such that the final PSFs of both images were circular Gaussians with final image qualities slightly worse than the worst original image. i.e.

$$\sigma_{\text{final}}^{x,y} = \sqrt{(\sigma_{\text{original}}^{x,y})^2 + (\sigma_{\text{smooth}}^{x,y})^2} \quad (1)$$

where $\sigma_{\text{final}}^{x,y}$ is chosen to be slightly larger than the sigma of the semi-major axis of the worst seeing image. These matched images were then divided by one another to produce a colour image. Colour images of each galaxy are shown in column 3 of Figure 1, with a zoom-in of the central $3'' \times 3''$ region shown in the following column. Note that the colour scales vary between the two columns. We could not construct a colour map of E+A.3 because the g -band image is saturated.

2.3 Spectroscopy

2.3.1 Observations

Our spectroscopic observations were obtained with the Gemini-South GMOS spectrograph in IFU mode. The observations were conducted in queue mode between 2005 September 2 and 2005 December 6. We used the B600 grating in combination with the g -filter resulting in a spectral coverage of $\sim 4100\text{--}5380 \text{ \AA}$ with a resolution of $\sim 1.9 \text{ \AA}$. We used the IFU in two-slit mode, which gives a rectangular field-of-view of $5'' \times 7''$ sampled by $1000 \times 0.2''$ individual lenslets. For each galaxy we obtained $4 \times 1020.5 \text{ s}$ dithered

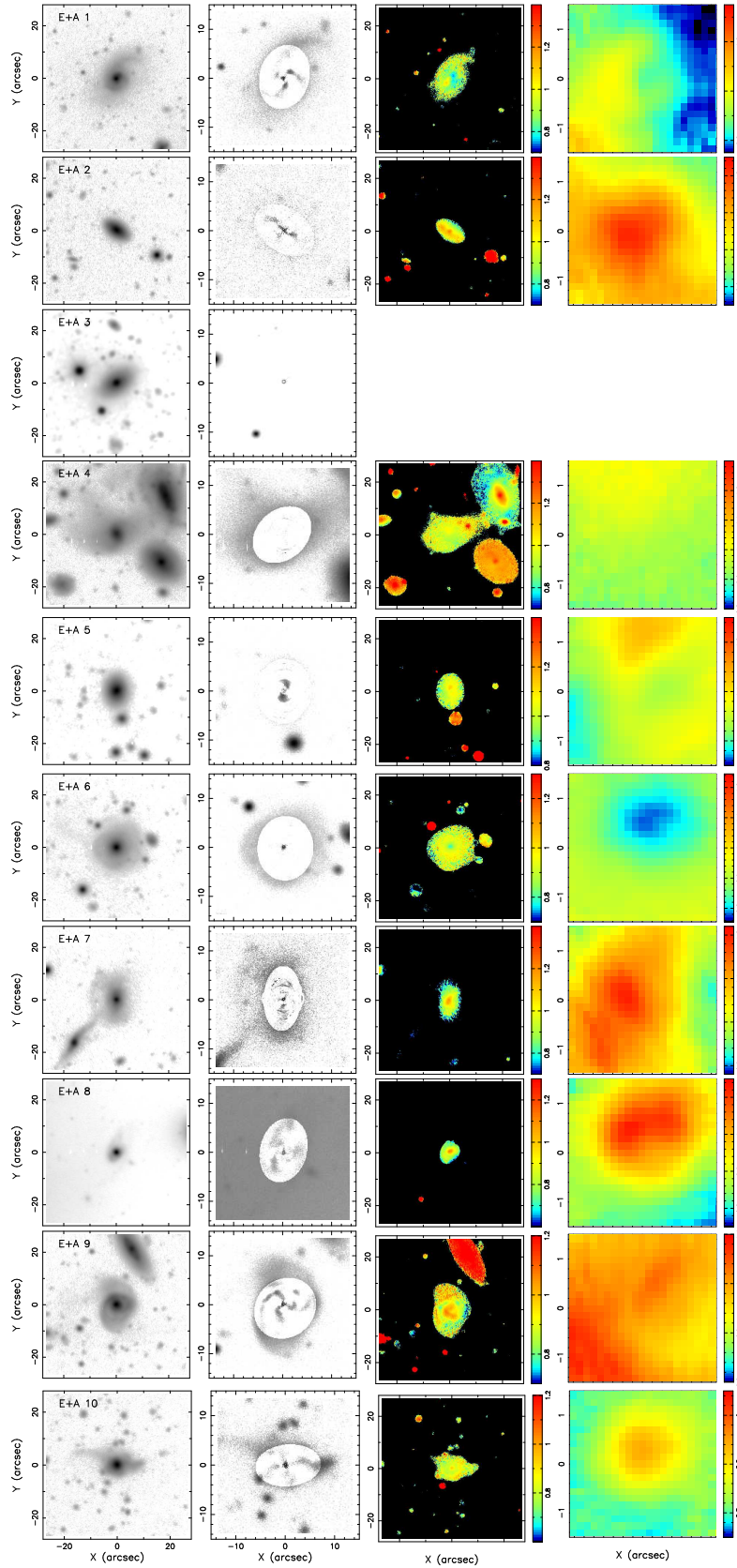


Figure 1. *Top to bottom:* E+A_1 to E+A_10. *left column:* g -band image; *2nd column:* residual image after subtraction of a model elliptical profile; *3rd column:* $g - r$ colour image; *right column:* colour image of the central $3''$. There is no colour image for E+A_3 because of saturation in the galaxy core in the g -band image as well as poor image quality in the r -band. Note: the spatial and colour scales vary between columns.

Table 1. List of target galaxies

Name	2dFGRS ID	RA	Dec	z	g	r	g - r	M _R	R _e (arcsec)	environment
E+A_1	TGS439Z075	00 29 10.97	-32 42 34.2	0.108	17.25	16.29	0.96	-22.34	1.44	Isolated
E+A_2	TGS271Z130	23 41 08.90	-28 55 25.4	0.082	17.83	16.75	1.08	-21.32	1.65	Group
E+A_3	TGS519Z227	02 33 10.60	-33 52 24.4	0.070	N/A	15.70	N/A	-21.96	1.63	Cluster
E+A_4	TGS520Z261	02 40 24.27	-33 25 50.6	0.035	17.64	16.61	1.03	-19.38	2.57	Group
E+A_5	TGS480Z208	22 18 22.99	-33 02 36.7	0.101	17.80	16.77	1.13	-21.66	1.70	Isolated
E+A_6	TGS358Z179	23 59 29.87	-30 16 21.9	0.120	17.24	16.36	0.88	-21.45	1.39	Group
E+A_7	TGS387Z032	02 15 40.52	-30 50 54.5	0.092	17.13	16.12	1.01	-22.17	1.60	Group
E+A_8	TGS539Z123	23 15 25.13	-35 12 59.1	0.196	17.71	16.75	0.96	-23.27	1.52	Isolated
E+A_9	TGS266Z090	23 10 46.57	-28 31 49.7	0.088	17.21	16.24	0.97	-21.99	1.64	Cluster
E+A_10	TGS350Z150	23 26 36.76	-30 19 27.4	0.158	17.86	16.97	0.89	-22.52	1.23	Isolated

Notes: Listed are the basic parameters of our E+A sample. Column 1 is an arbitrary ID and Column 2 is the 2dFGRS ID. The remainder of the columns are (from left to right): target right ascension and declination (J2000), redshift, *g*-band magnitude, *r* magnitude, *g* - *r* colour, absolute R magnitude inclusive of a *k*-correction (Wild et al. 2005), the effective radius measured from the imaging using the IRAF ELLIPSE TASK, AND GALAXY ENVIRONMENTAL CLASSIFICATION FROM BLAKE ET AL. (2004).

Table 2. Summary of GMOS observations

Name	g exptime (s)	FWHM (arcsec)	r exptime (s)	FWHM (arcsec)	spec exptime (s)	observed λ (Å)	rest λ (Å)
E+A_1	1262	0.88	1262	0.76	4082	4122–5380	3720–4855
E+A_2	1262	0.92	1262	0.79	4082	4122–5380	3810–4972
E+A_3	1262	0.57	1262	1.15	4082	4122–5380	3852–5028
E+A_4	2524	1.14	2524	1.08	N/A	N/A	N/A
E+A_5	2103	1.16	1262	1.23	4082	4122–5380	3744–4886
E+A_6	1262	0.98	1262	1.02	4082	4122–5380	3680–4803
E+A_7	1262	0.95	1262	0.96	4082	4122–5380	3775–4926
E+A_8	1682	0.95	1262	0.83	N/A	N/A	N/A
E+A_9	1262	1.02	1262	0.99	4082	4122–5380	3788–4945
E+A_10	1262	1.05	1262	1.00	4082	4122–5380	3559–4646

Notes: Column 1 is galaxy ID. Columns 2 and 3 are the *g*-band exposure time and seeing. Columns 4 and 5 are the *r*-band exposure times and the corresponding seeing. Column 6, 7 and 8 are the spectroscopic exposure time, observed spectral wavelength coverage and rest-frame spectral wavelength coverage.

exposures, resulting in a total exposure time for each target of 4082 s. Only 8 of our 10 targets were observed spectroscopically. A summary of the spectroscopic observations is given in Table 2.

2.3.2 Data reduction

The spectroscopic data were reduced using standard IRAF routines. Firstly, the flat field spectra were overscan-subtracted and trimmed using the IRAF GEMINI package task GIREDUCE. The flat field fiber spectra were traced, extracted and the individual CCDs mosaiced using the GFEXTRACT task. The task GFRESPONSE was used to calculate the relative fiber throughputs from the flat field spectra. Arc images were then matched to their temporally nearest flat-field image and reduced in a similar manner but using the flat-field to define the spectroscopic apertures and traces. Following this, the wavelength solution was determined interactively using the GSWAVELENGTH task. The science spectra were overscan subtracted, trimmed, extracted using the trace of the nearest flat-field image, wavelength calibrated using the appropriate wavelength solution and corrected for variations in the relative fiber throughput using their corresponding response images.

At this point, inspection of the extracted 2-D spectra revealed several problems. There were throughput discontinuities in the wavelength direction where the different CCDs had been mosaiced together. There was also a discontinuity in the 'spatial' direction of the 2-D spectra corresponding to the cross over between the 2 slits. Further, looking at the spectra from sky fibers (and fibers corresponding to the outer part of the science IFU which are expected to have little contribution from the target galaxy) revealed a gradient in throughput with aperture number (spatial axis of the 2-D spectrum). This gradient appeared (and had the same sense) in both halves of the 2-D spectra corresponding to the two separate slits. These gradients were fitted, in each individual exposure, with a linear function on either side of each discontinuity and then divided out to give an approximately uniform level in the sky spectra. The sky spectra corresponding to each slit were then averaged and sky subtraction was performed on all spaxels¹. The accuracy and systematics in the sky subtraction were checked by examining both the sky-subtracted sky spectra and also (importantly) the

¹ A spaxel is the SPAtial piXture ELement of the instrument; in this case the IFU lenslet array

sky-subtracted spectra from the outer regions of the target galaxy IFU, which have essentially no signal from the galaxy, and hence are a good indication of how well our reduction and sky subtraction has worked for our galaxy spectra. In general this procedure worked well, however, small residual offsets and gradients in the sky-subtracted sky spectra remained. At this point data cubes were constructed for each IFU observation using the task GFCUBE. The data were re-sampled spatially by this procedure and the resulting data cube had spatial pixels which were square with $0.2''$ sides. The data cubes corresponding to individual dithered exposures for each target were shifted and averaged into a single data cube. The original observations were performed with a square dither pattern with each individual exposure offset by $1''$. This dither pattern between exposures was checked a posteriori by collapsing the cubes of individual exposures along the spectral direction and comparing the resulting images. This confirmed the accuracy of the dither pattern to sub-spaxel accuracy and means any smearing of the image quality during combination will be small compared to the seeing. Therefore we were able to combine the individual data cubes by shifting an integer number of spaxels (i.e. $5 \times 0.2''$ spaxels) before combining the spectra using the IRAF task SCOMBINE. Each spectrum was then cleaned of any remaining cosmic rays using the IRAF task LINECLEAN. The residual offsets described above could be seen in the final data cube as additive offsets between different columns of IFU elements and these were removed by subtracting off the average spectrum from the two outermost lenslets from all other lenslets in that column. After this procedure, examination of those spectra in the data cube, which had no discernible signal from the galaxy, revealed a well behaved sky subtraction with little sign of systematics present.

The systematics in the sky subtraction can be quantified by measuring the rms of the mean flux in spaxels expected to have no contribution from the object. This can then be compared with the random noise by measuring the mean of the rms scatter in those spaxels. For our data the ratio of these is in the range 19 to 26 per cent, implying that the systematics in the sky subtraction are small compared with the random errors. A relative flux calibration was performed using observations of a flux standard star taken with the same set up as the science observations, which are done as part of the standard calibrations at Gemini Observatory.

3 PHOTOMETRIC CHARACTERISTICS

3.1 Isophotal profiles

We constructed isophotal surface brightness profiles using the IRAF task ELLIPSE. The g -band surface brightness profiles are shown in Figure 2. The r -band profiles (not shown) are qualitatively similar. The inner parts of the profiles out to $\sim 0.8''$ are flattened by convolution with the seeing disk. At larger galacto-centric radii, the profiles appear like typical early-type galaxies with $r^{\frac{1}{4}}$ -like profiles (linear on a $r^{\frac{1}{4}}$ horizontal axis). The exception is the isophotal profile of E+A_2 (and to a lesser extent E+A_5) which appears more typical of a disk i.e. a strong downward concavity in the surface brightness profile. An $r^{\frac{1}{4}}$ law fit to the data beyond $1R_e$ is shown as the red line in Figure 2. The profiles display

some irregular structure expected for objects which have disturbed morphologies (see Figure 1), which is also evidenced by the position angles and ellipticities of the best fitting ellipse changing with semi-major axis distance. These results are generally consistent with the HST study of Yang et al. (2008) which found E+A galaxies from the Zabludoff et al. (1996) LCRS sample to be predominantly early-type systems but with a greater than normal level of asymmetries.

3.2 Morphological properties

Several previous studies have found E+A samples to have a large fraction of morphologically disturbed members (Zabludoff et al. 1996; Yang et al. 2004; Blake et al. 2004) and nearby companion galaxies (Goto 2005). A primary aim of acquiring deep imaging with an 8-m class telescope of our sample was to search for the signatures of interactions and mergers in the form of faint tidal tails and debris. Inspection of the g -band images (see column 1, Fig. 1), as indeed the r -band images of our sample reveals that six out of ten galaxies in the sample (E+A_1, E+A_4, E+A_7, E+A_8, E+A_9, E+A_10) show either tidal bridges or tails or clearly disturbed morphologies with at least three of these apparently currently undergoing an interaction with a companion (E+A_4, E+A_7, E+A_9). The remaining four galaxies appear like undisturbed early-type systems.

Table 3 contains a summary of the morphological properties of the sample. The Hubble classifications listed in column 2 of the Table were determined visually from our r -band GMOS images. This was done by one of us (W.J.C.) using the same approach and system described in Blake et al. (2004), and which is based on the methodology adopted by the ‘‘Morphs’’ collaboration in their HST-based study of the morphologies of the galaxy populations in distant clusters (Smail et al. 1997). One small modification was required here and that was to adopt a classification denoted by ‘‘S0a’’, to indicate galaxies where it was impossible to distinguish them between an S0 and an Sa galaxy, due to them showing tentative but not convincing evidence for harbouring spiral arm structure. As can be seen in Table 3, 40 per cent of our sample have an S0a classification, and indeed our E+A sample is quite striking for its very narrow range in Hubble type (S0-S0a-Sa).

In column 2 of Figure 1 we show the results of subtracting a smooth elliptical model from the images in an attempt to reveal any faint sub-structure more clearly. The elliptical model was produced with the IRAF ELLIPSE and BMODEL tasks and we allowed the position angle and ellipticity of each isophotal ellipse to vary freely. In several cases the tidal/debris structures can be seen more clearly and further toward the galaxy centers. E+A_2 and E+A_5 reveal disk-like structures along their major axes consistent with the shapes of their isophotal profiles.

We find an even higher rate of morphological disturbance than the original Zabludoff et al. (1996) study of the LCRS which found 5 out of 21 (~ 24 per cent) galaxies showed signs of disturbance. This difference is likely due to the limited depth of the Digital Sky Survey (DSS) imaging used. Indeed many of the tidal features in the imaging presented here are of too low surface brightness to be detected in the DSS which was one of the motivations for acquiring deeper imaging.

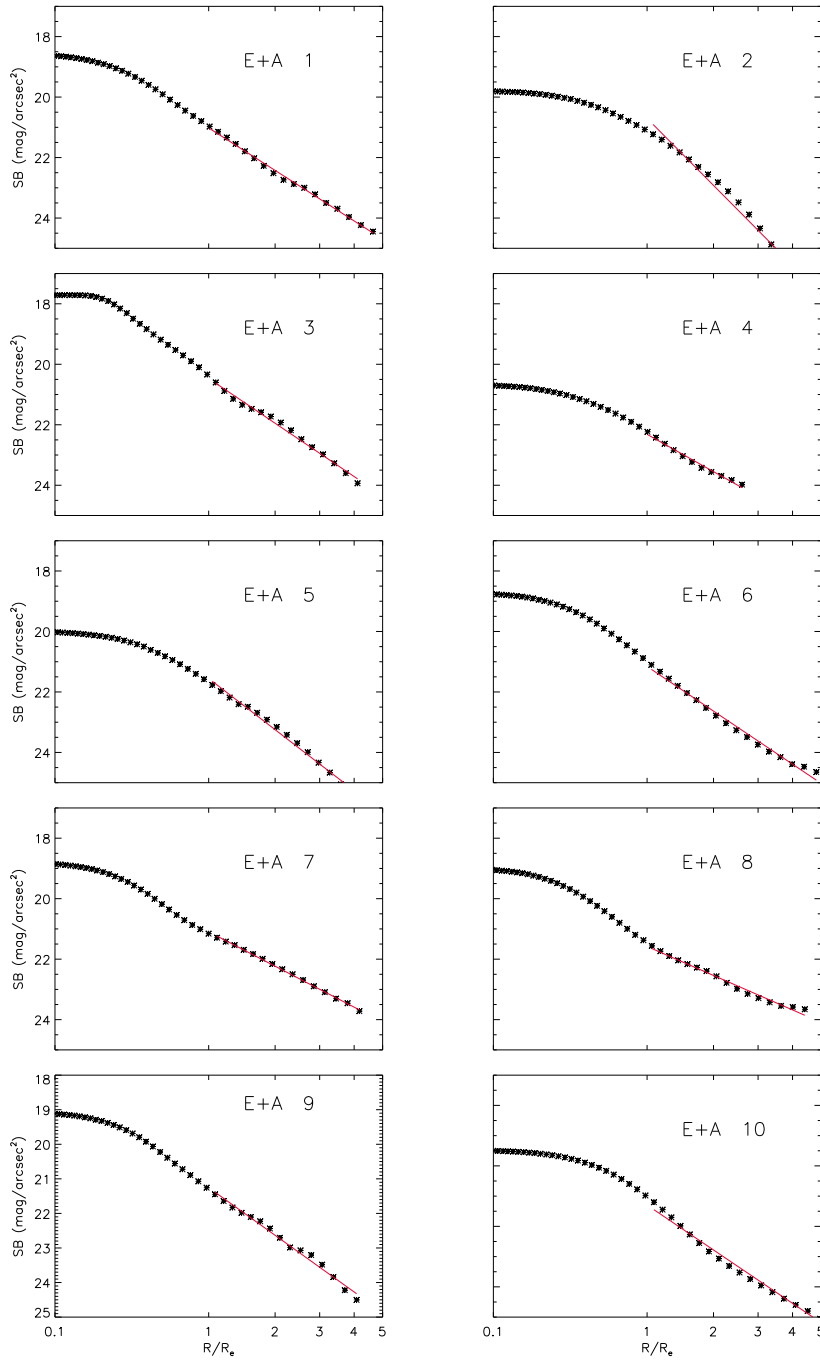


Figure 2. g -band surface brightness profiles of all ten galaxies in the sample plotted on an $r^{\frac{1}{4}}$ abscissa and given in units of the effective radius. The profiles are flattened in the inner $\sim 1''$ by convolution with the seeing disk – the saturation in the centre of E+A_3 is also evident. At larger radii they are generally consistent with an $r^{\frac{1}{4}}$ law elliptical profile – overplotted as a *red line*. There are some deviations from $r^{\frac{1}{4}}$ profiles; E+A_2 in particular has a more exponential (disk-like) profile.

3.3 Colour morphologies

We constructed two dimensional $g - r$ colour maps as outlined in Section 2.2.2. These maps are shown in the two right-most columns in Figure 1 and show a $60'' \times 60''$ map (3rd column) and a $3'' \times 3''$ map of the galaxy core (4th column). The colour distributions in the galaxy cores are varied with the most common property being the presence

of a red nuclear core. The cores are red only in a relative sense with respect to the outer parts of the galaxy – the absolute colours of the galaxies are blue in agreement with their E+A status. A red core is evident in 4 of the 9 galaxies (E+A_2, E+A_7, E+A_8, E+A_10). Two galaxies have irregular color structure in their centres (E+A_1, E+A_5) and two little structure at all (E+A_4, E+A_9) whilst one galaxy in our sample shows a clear blue core (E+A_6). This is in

Table 3. Morphological properties

Name	Morph	Neighbour	Disturbed/Tidal	centre col	col grad	Environment	Comment
E+A_1	Sa	No	Yes	Irregular	P	Isolated	Tidal arm or bridge
E+A_2	S0a	No	No	Red	F	Group	Normal/isolated
E+A_3	S0	No	No	N/A	F	Cluster	Normal/isolated
E+A_4	Sa	Yes	Yes	None	P	Group	Compact group/Lots of diffuse light
E+A_5	S0a	No	No	Irregular	F	Isolated	Normal/isolated
E+A_6	S0a	No	No	Blue	P	Group	Normal/isolated
E+A_7	S0a	Yes	Yes	Red	N	Group	Neighbour/tidal bridge
E+A_8	S0	No	Yes	Red	N	Isolated	Tidal tail
E+A_9	Sa	Yes	Yes	None	F	Cluster	Neighbour/disturbed
E+A_10	S0	No	Yes	Red	F	Isolated	Tidal tail

Notes: Listed are the morphological and colour properties of our sample. Column 1 is galaxy ID, Column 2 is a by eye morphological classification, Columns 3 and 4 indicate the presence or otherwise of near neighbours and tidal features. Columns 5 and 6 are the core colour and colour gradient classifications. Column 7 is the environmental classification from Blake et al. (2004) and column 8 is a comment on specific photometric properties.

contrast to the recent study of Yang et al. (2008) using HST imaging of 21 E+A galaxies of which 6 had compact blue cores with very steep profiles. These structures, however, are on scales much smaller than our resolution element. Some of these profiles have complicated core color structures and it is unclear how these color morphologies would appear at our resolution given the flux and area variation with radius, or even whether the cores would be red or blue (see e.g. EA12, EA02 and EA09 in Figure 6 of Yang et al. (2008)). While both samples display diversity in colour morphology with examples of blue, red and irregular cores our sample does appear to have a higher fraction of red core galaxies even if direct comparison is difficult.

3.4 Colour gradients

On larger scales, outside the core, we still see a diversity in behaviour. In Figure 1 several galaxies have negative colour gradients becoming bluer with increasing galacto-centric radius (e.g. E+A_7) whilst others have little sign of a gradient at all (e.g. E+A_10) or have large scale patchiness in their colour distribution (e.g. E+A_9). We use the IRAF ELLIPSE task to examine the nature of the large scale radial (semi-major axis) colour gradients. This is done by fitting elliptical isophotes to the PSF matched g - and r -band images at regularly spaced semi-major axis lengths. The results for our sample are shown in Figure 3. On these scales we again see variation in the radial color profile shapes. We use the same classification scheme that Yang et al. (2008) use to classify their large scale colour gradients by categorizing profiles as positive, negative or flat/variable. This colour gradient classification for each galaxy is listed in Table 3. We classify two galaxies as having negative colour gradients (20 per cent), five to be flat/variable (50 per cent) and three to be positive (30 per cent). These can be compared with Yang et al. (2008) who find 29, 19, and 51 per cent of their sample to be negative, flat/variable and positive, respectively. Note, however, while the positive gradient galaxies have mild slopes and are not too dissimilar to the flat gradient galaxies the two most striking gradients (E+A_7 and E+A_8) are both negative. This is true for many examples in the Yang et al.

(2008) sample as well, where the slope of the profile outside the core could easily be classified as flat rather than positive. Qualitatively, and taken as a whole, the large scale colour gradient behaviour in the two samples is quite similar (c.f. Figure 3 with their Figure 6). Likewise, Yamauchi & Goto (2005) find the majority of their E+A sample to have positive colour gradients – again with slopes that are generally quite shallow.

4 SPECTROSCOPIC CHARACTERISTICS

4.1 IFU data cubes

The data reduction procedure outlined in Section 2 produces for each target galaxy a data-cube with spatial dimensions of $7'' \times 5''$ with $0.2''$ spaxels and a wavelength coverage of $\sim 4122 < \lambda < 5380 \text{ \AA}$ sampled by 1410 spectral pixels.

There is little galaxy signal in the outer parts of the IFU and even spatially binning over large areas in the very outskirts is unable to produce a reasonable quality spectrum. We therefore restrict our analysis to the central $3''$ region where the signal-to-noise ratio is sufficient for a robust analysis.

4.2 Integrated spectra

We first produce a high quality integrated spectrum for each of our target galaxies by collapsing the data cube in the spatial directions. That is, we co-added all of the individual spaxels together weighted by their variance. These spectra are shown in Figure 4 where they have been adjusted to their rest-frame by division of the wavelength scale by $1+z$.

4.3 Line strength indices

We measure line strength equivalent widths on the Lick/IDS system (Worthey & Ottaviani 1997; Trager et al. 1998). This system uses a flux summing technique whereby a central bandpass containing the line is flanked by two bandpasses, one each to the red and blue side of the spectral line. The mean ‘continuum’ level in each of the bands adjacent to the

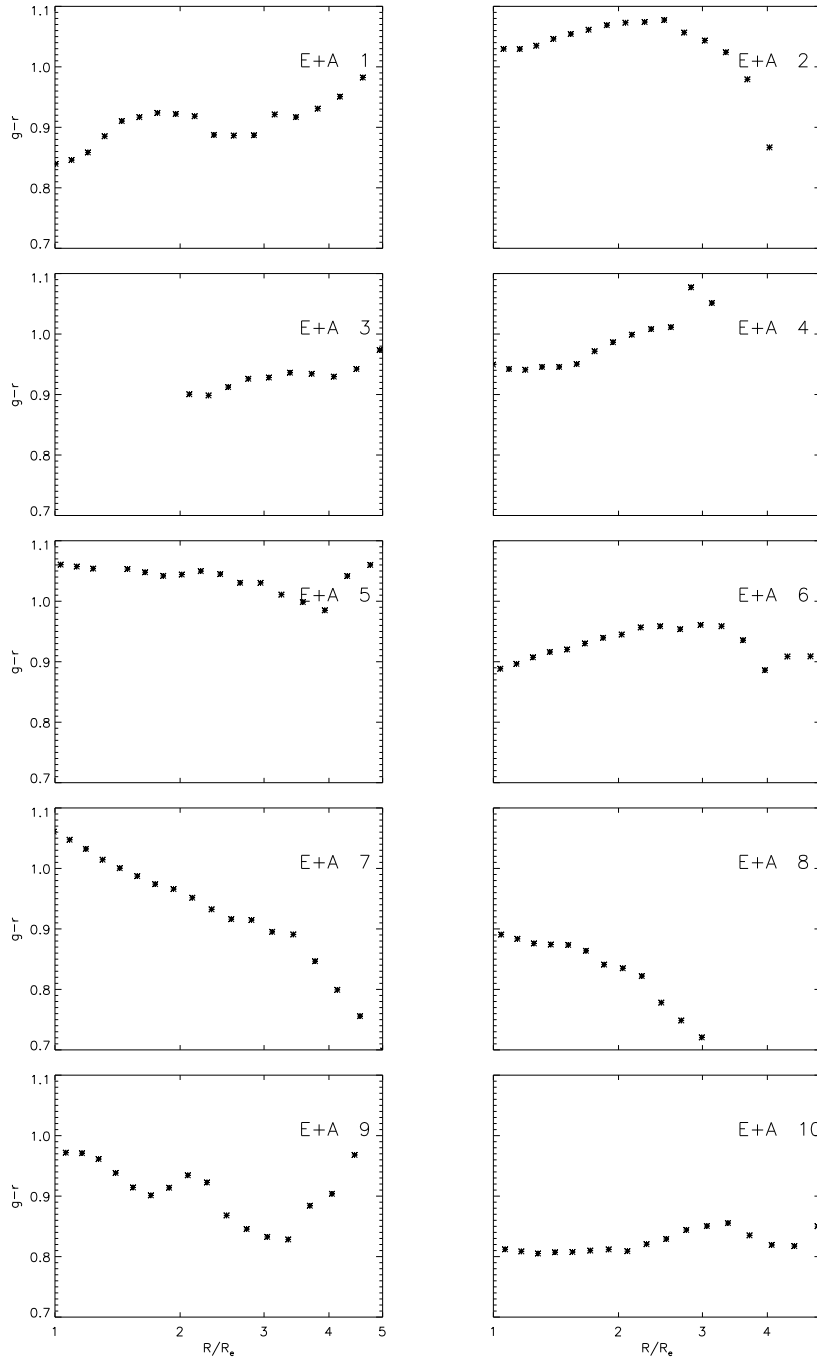


Figure 3. $g - r$ colour gradients along the semi-major axis. Gradients are shown beyond $1 R_e$ except for E+A-3 which is shown only beyond $2 R_e$ due to saturation in the galaxy centre and poor seeing in the r-band image.

line is measured and a straight line extrapolation between the two is used as a measure of the interpolated continuum level in the central bandpass. The ratio of the summed counts in the central bandpass to the expected height of the continuum is used as the estimate of the line equivalent width. Prior to measuring the indices the spectra were broadened to Lick resolution by convolution with a wavelength dependent Gaussian such that the quadrature sum of the Gaussian width and the instrumental resolution were equal to the Lick resolution ($\sim 9 \text{ \AA}$ depending on the pre-

cise wavelength). The line index strengths were corrected for smearing effects due to the intrinsic velocity dispersion of the galaxies following the prescription of Kuntschner (2004). We also correct for differences in the measured equivalent widths and the Lick system using the known offsets for data with flux calibrated continuum (Norris et al. 2006).

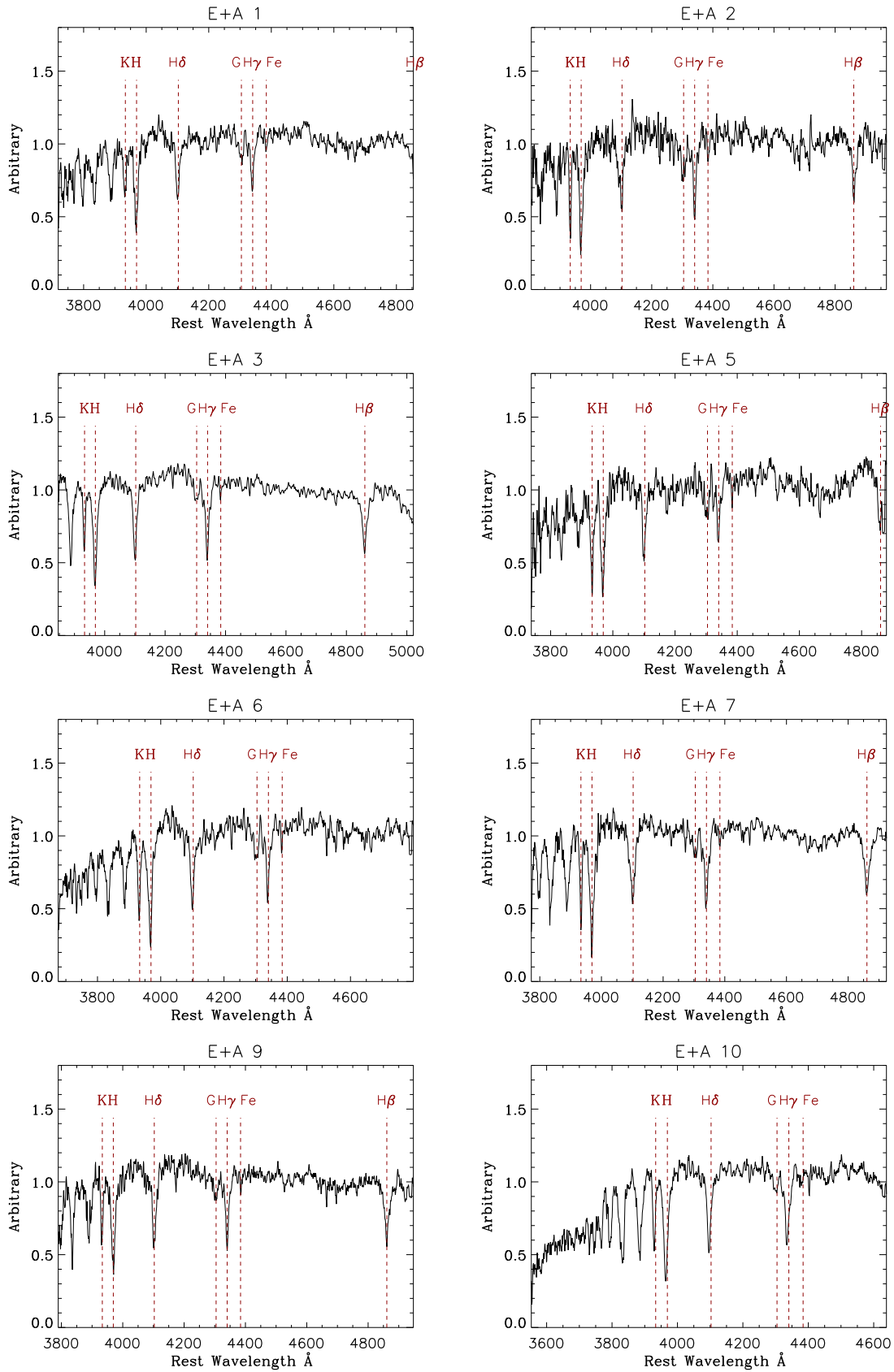


Figure 4. Integrated spectra made by combining the IFU data spatially. Galaxy names are shown as the title in each panel.

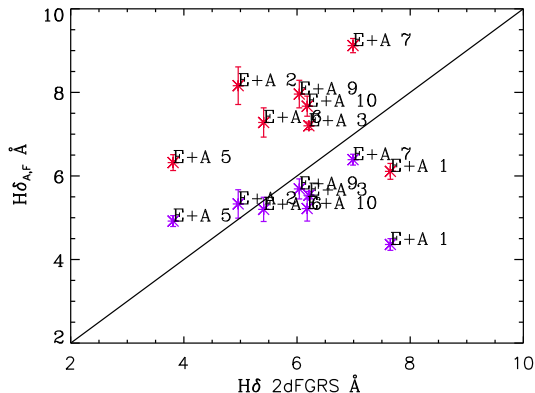


Figure 5. The $H\delta$ equivalent width measurements from our spatially integrated GMOS spectroscopy compared with the original measurements that were made from the 2dFGRS spectra using Gaussian line fitting. The red and blue points show the $H\delta_A$ and $H\delta_F$ measurements, respectively. The black line shows the one-to-one relationship. The $H\delta_A$ index returns larger equivalent widths which appear like a constant offset whilst the $H\delta_F$ index more closely resembles the line-fit values.

4.4 Global spectral properties

We first re-examine the key spectral line diagnostic for our galaxy sample to confirm their original classification from the 2dFGRS spectroscopy. All the galaxies studied are clearly dominated by young stellar populations evidenced by the strong Balmer series absorption clearly visible in Figure 4. The defining spectral line for E+A galaxies is the $H\delta$ absorption line. In Figure 5 we compare the previously measured $H\delta$ absorption line equivalent widths from 2dFGRS spectra using a line-fitting technique (Lewis et al. 2002) with the values derived from our spatially integrated spectra using the line-summing technique described above. We utilize the two commonly applied index definitions for $H\delta$; the $H\delta_F$ and $H\delta_A$ indices (Worthey & Ottaviani 1997). The $H\delta_F$ definition has a narrow central bandpass designed as a probe of F-star populations whilst the $H\delta_A$ definition has a wider central bandpass designed to include the broader A-star light – seemingly a more natural definition for E+A galaxies.

In Figure 5 we compare our new index measurements with those previously derived from the 2dFGRS spectra (Lewis et al. 2002; Blake et al. 2004). The $H\delta_A$ index generally results in larger equivalent widths than those originally derived via line-fitting but the relative line strengths between objects are similar between the two different sets of observations and measurement techniques. The $H\delta_F$ index returns values similar to the original line-fit results. Our selection from the 2dFGRS sample of Blake et al. (2004) is 100 per cent successful in selecting E+A galaxies.

In Figure 6 we show some age-metallicity diagnostic diagrams using Lick index measurements of the Balmer absorption lines $H\delta$, $H\gamma$ and $H\beta$ along with the metallicity indices Fe4383 and C24668. The over-plotted predictions of single stellar population (SSP) models are taken from Thomas et al. (2003, 2004) and assume solar abundance ratios. The position of our target galaxies with respect to the grids confirm their young luminosity-weighted ages (scattered around ~ 0.5 Gyr) consistent with their E+A classifi-

cation. Our selection criteria of strong $H\delta$ absorption without the presence of emission lines basically select galaxies where the Balmer absorption strength is maximized (model prediction ~ 0.4 Gyr). Our sample shows a range of luminosity weighted metallicities from about solar to several times solar metallicity. Due to the sparsity of suitable Lick indices in our rest wavelength range, attempts to obtain a meaningful estimate of the abundance ratios failed and hence we assume solar values.

4.5 Adaptive spatial binning

There is large variation in the signal-to-noise ratio of the individual spectra within each data cube. For the most part the signal-to-noise ratio decreases rapidly with galactocentric radius and in general the signal-to-noise ratio of an individual spaxel is insufficient for quantitative analysis. As a result, we need to bin the data-cube spatially to increase the signal-to-noise ratio in each spectrum. To do this we use the Voronoi spatial binning method of Cappellari & Copin (2003). In this scheme the data are adaptively binned in order to achieve a predefined signal-to-noise ratio across the full area of the IFU. In practice, this means binning over large areas where the signal is low – usually the galaxy outskirts – while using small bins where the signal is high – usually in the centres of the galaxies. We choose different final signal-to-noise ratios for each galaxy depending on the intrinsic quality of the spectra for that galaxy. The chosen final, per spatially binned element, signal-to-noise ratios range from 5 \AA^{-1} for the lowest quality data to 15 \AA^{-1} for our brightest target.

4.6 Spatially resolved line index measurements

We made spatially-resolved line index measurements using the adaptively binned data. The $H\delta_A$ equivalent width maps for our sample are shown in Figure 7. These maps generally reveal a uniformly high Balmer absorption line equivalent width with little evidence for radial gradients present. It should be noted, however, that our data cover only the central $3'' \times 3''$ which corresponds to a maximum galactocentric radius of only ~ 2 to 5 kiloparsecs. Previous long-slit or photometric studies have claimed cases of E+A galaxies having a young population spread over these scales with radial gradients seen only on larger scales (Goto et al. 2008). This scale of a few kiloparsecs is also the scale a merger/interaction-induced starburst is expected to be concentrated on (Bekki et al. 2005). Furthermore, the $3''$ scale is comparable to the expected seeing disk ($\sim 1''$) which has the effect of smoothing out any radial variations. Therefore, while we see uniformly strong $H\delta$ absorption across the central few kiloparsecs we cannot rule out the presence of gradients at larger galactocentric radii. The lack of significant gradients is more clearly displayed in Figure 8 where rather than use the adaptively binned data we have binned the spectra in three concentric annuli and measured the $H\delta$ line equivalent width. The radial plots reveal no clear radial trends.

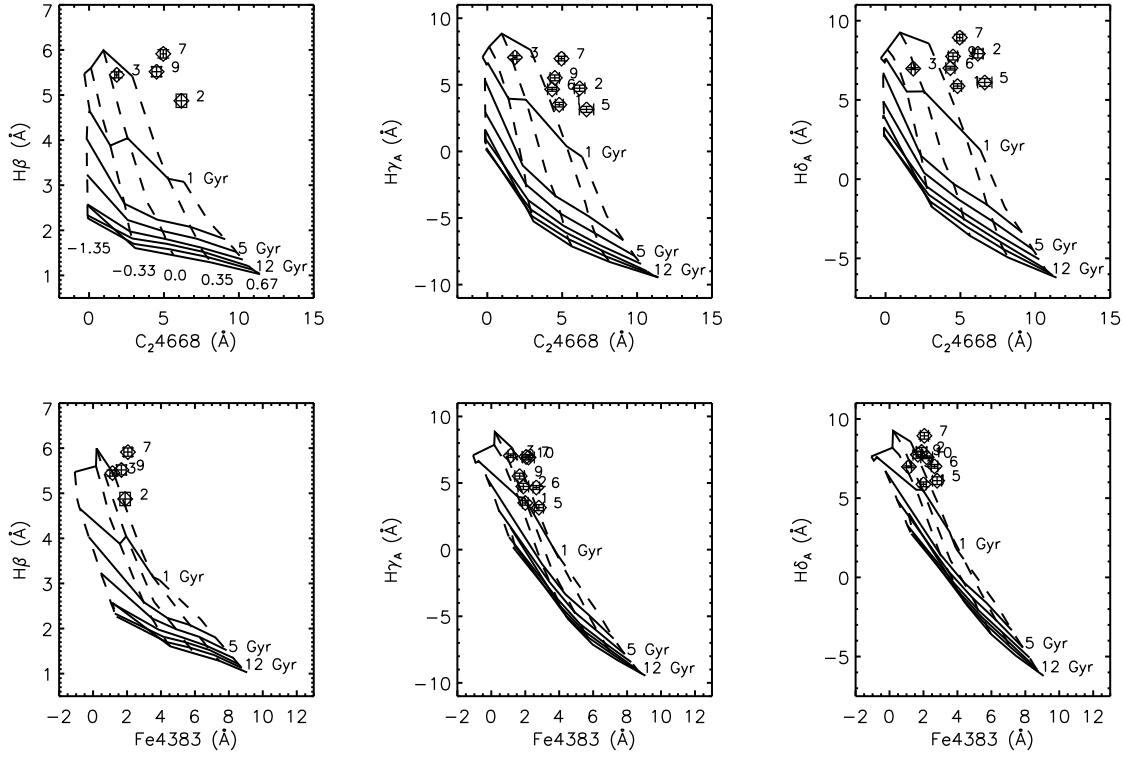


Figure 6. Age metallicity diagnostic diagrams confirming the young luminosity weighted ages of our E+A sample. Galaxy names are indicated by numbers. Over-plotted are models by Thomas et al. (2003, 2004) with solar abundance ratios. The models span a range in metallicity $[Z/H] = -1.35$ to $+0.67$ (dashed lines), and solid lines indicate ages from top to bottom of 0.4, 1, 3, 5, 8, 10, 12 and 15 Gyr, respectively.

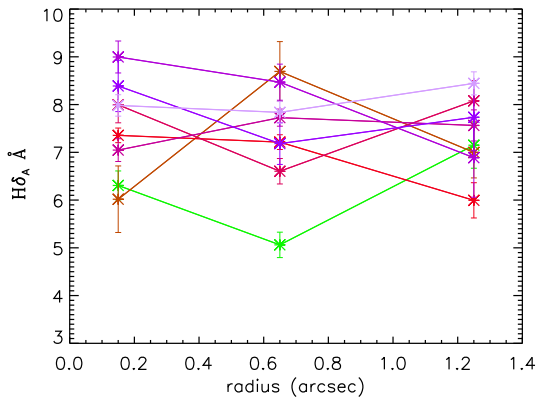


Figure 8. $H\delta$ radial gradients measured from annular binned spectra.

4.7 Template fitting

Rather than utilizing just the information obtained by measurement of discrete line indices, we can use all the information contained in the spectroscopic data by fitting the entire spectrum simultaneously. By doing so, we can simultaneously gather information on the stellar populations, the streaming velocity and velocity dispersion of individual spatial elements of our target galaxies. The accuracy of the extraction of kinematics from the data is greatly increased

since many lines are used simultaneously in measuring the redshift and line-of-sight velocity dispersion.

As templates for fitting, we use the single-age single-metallicity stellar population synthesis models of Vazdekis et al. (2007). The stellar population spectral energy distributions are constructed from the MILES empirical stellar library (Sánchez-Blázquez et al. 2006). We use a range of templates in the fit ranging in age from 0.1 Gyr to 13 Gyrs. The age difference between templates is ~ 0.1 Gyr for ages of less than 1 Gyr whilst we use a sparser sampling in age for the older population templates. Solar metallicity is assumed for the young templates (< 1 Gyr) and a variety of metallicities are allowed for the old stellar population templates. The reason a variety of metallicities are not used for the young templates is because the spectra are much more sensitive to age than metallicity in this regime, and including more freedom in metallicity does not ultimately improve the fit. A list of all templates allowed in the fitting routine is given in Table 4.

The fitting is performed using a penalized pixel fitting algorithm (Cappellari & Emsellem 2004) which fits the spectrum in pixel space using the combination of a number of input user-supplied templates and simultaneously fitting for redshift and velocity dispersion. Prior to fitting, the science spectra are smoothed from their intrinsic 1.9 \AA spectral resolution to have the same intrinsic spectral resolution as the template spectra i.e. 2.3 \AA (FWHM).

In Figure 9 we show an example spectrum of a single,

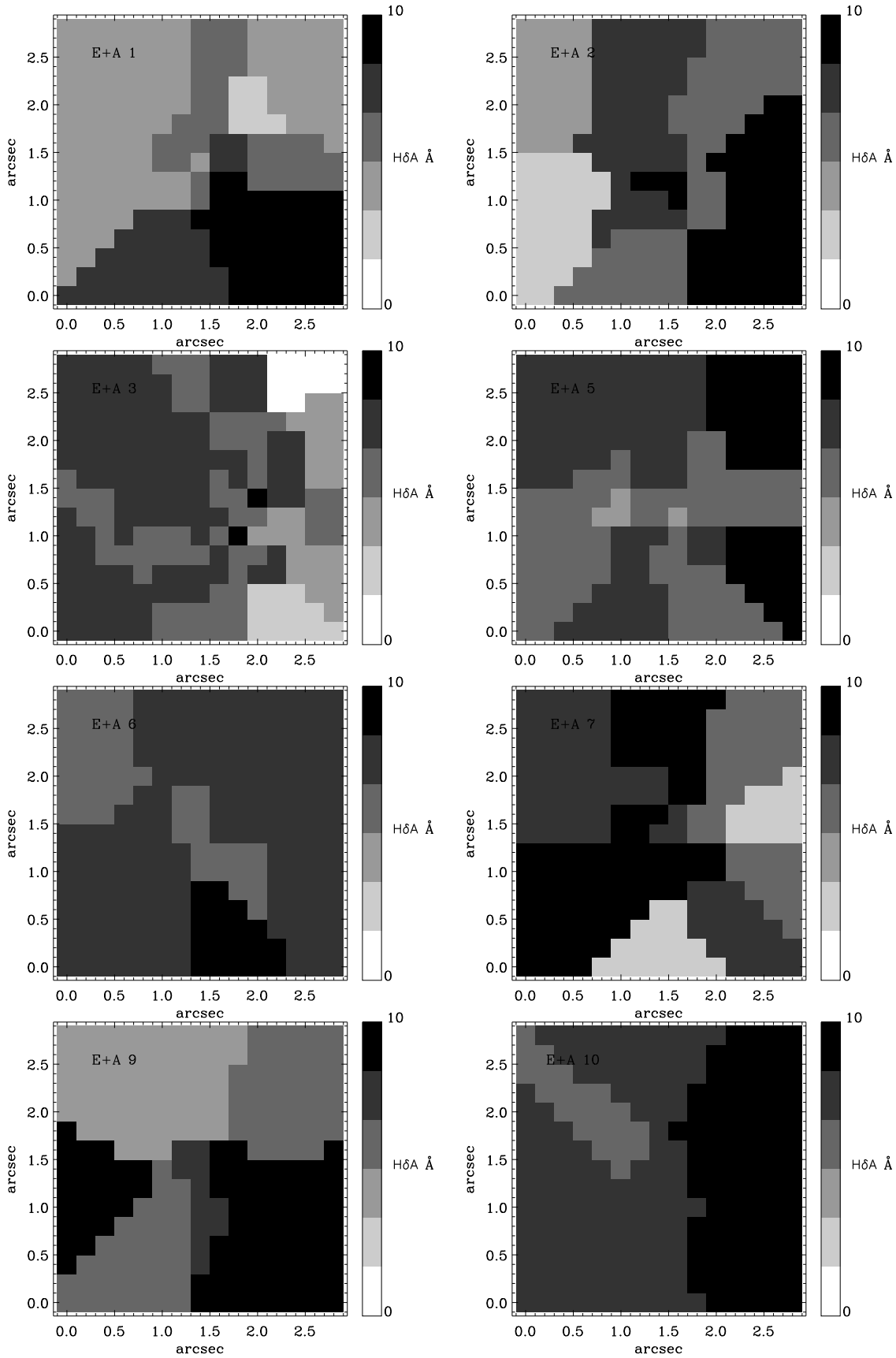


Figure 7. H δ A equivalent width maps measured in adaptively binned regions. The sample exhibits uniformly strong absorption over the central 3".

Table 4. Stellar population templates (from Vazdekis et al. 2007) used for fitting our E+A spectra.

Template no.	Age (Gyr)	Metallicity
1	0.10	0.0
2	0.20	0.0
3	0.32	0.0
4	0.40	0.0
5	0.50	0.0
6	0.71	0.0
7	0.89	0.0
8	4.47	-1.68
9	4.47	-1.28
10	4.47	-0.68
11	4.47	-0.38
12	4.47	0.0
13	4.47	0.2
14	7.98	-1.68
15	7.98	-1.28
16	7.98	-0.68
17	7.98	-0.38
18	7.98	0.0
19	7.98	0.2
20	12.59	-1.68
21	12.59	-1.28
22	12.59	-0.68
23	12.59	-0.38
24	12.59	0.0
25	12.59	0.2

adaptively-binned spatial pixel along with the best fitting model spectrum produced by the above technique. The observed spectra are generally well fitted by model spectra produced in this way and the quality of the data and the goodness of fit shown in Figure 9 are fairly typical.

4.8 Stellar population

The composite model spectra that best fit our observed E+A spectra are those dominated by young stellar population templates (< 1 Gyr). In fact, for the most part, inclusion of older stellar templates, whilst often given small non-zero weighting by the penalized pixel fitting algorithm, does not improve the fit to the data in a statistically significant way. That is, at the signal-to-noise ratio of the data, we are unable to detect any contribution from an old stellar population in the spectra. An example of this is shown in Figure 9. In the top panel is the best fit to the spectrum of one spatial pixel using all the input templates from Table 4 and in the bottom panel is the best fit using only stellar populations synthesis templates with ages of less than 1 Gyr (i.e. templates 1-7). There is little difference between the two fits. As an example of the lack of contribution from the old stellar templates the mean difference (per spaxel) in the χ^2/DOF values for E+A_10 returned by fitting with the different sets of templates is ~ 0.09 . At this point we caution that our spectral analysis only really constrains the young population which is the dominant contributor to the stellar light but not the stellar mass.

We constructed a pseudo ‘age map’ of the young population by taking the weighted age of the best fitting SSP

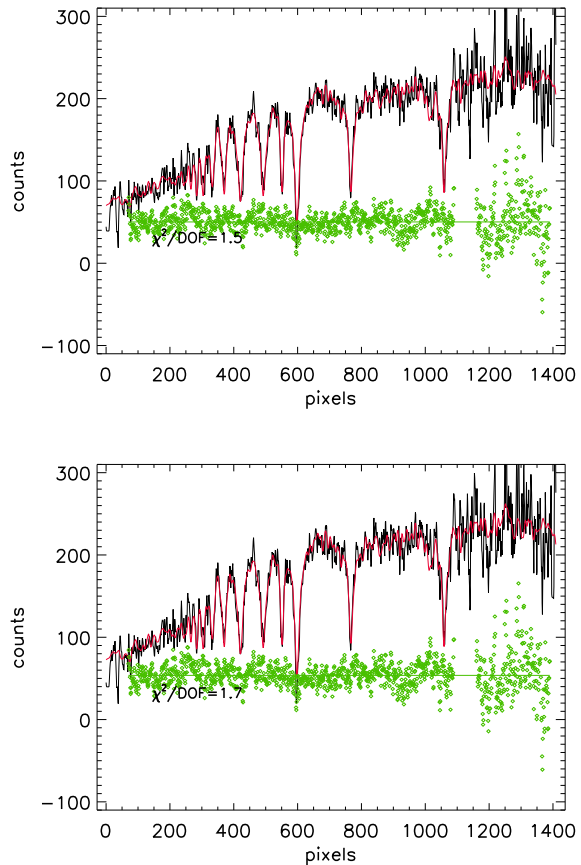


Figure 9. *Top panel:* The spectrum of a single adaptively-binned spatial pixel of E+A_10 where we have Voronoi binned to a signal-to-noise ratio of 15. The *black line* is the data and the *red line* is the best fit using all the templates in Table 4. The residuals are shown as *green points*. The pixel values where no residuals are plotted have been excluded from the fit due to poor data quality in these regions. *Bottom panel:* same as *top panel* but using only the templates with ages less than 1 Gyr in the fit

templates from each spaxel. These maps are shown in Figure 10. The age maps are somewhat noisy, although there are a couple of examples of possible age gradients across the field-of-view (e.g. E+A_2, E+A_7). The sample generally have ‘weighted ages’ of ~ 0.5 Gyr, perfectly consistent with their E+A status and consistent with the age-metallicity diagnostics of their global spectra in Section 4.4. Radially averaged ‘ages’ are plotted in Figure 11 and there is no sign of significant radial trends.

4.9 Internal kinematics

The stellar kinematics of an E+A galaxy may offer the best clues to what represent plausible formation mechanisms. For an equal mass merger the remnant should usually be dynamically pressure supported (NGZZ; Bekki et al. 2005). However, for unequal mass mergers and tidal interactions, rotation of the young stellar population is expected in most cases (Bekki et al. 2005). Here the probability of a rotating remnant increases with increasing mass ratio of the merger progenitors (Bournaud et al. 2008). Likewise, if ‘normal’

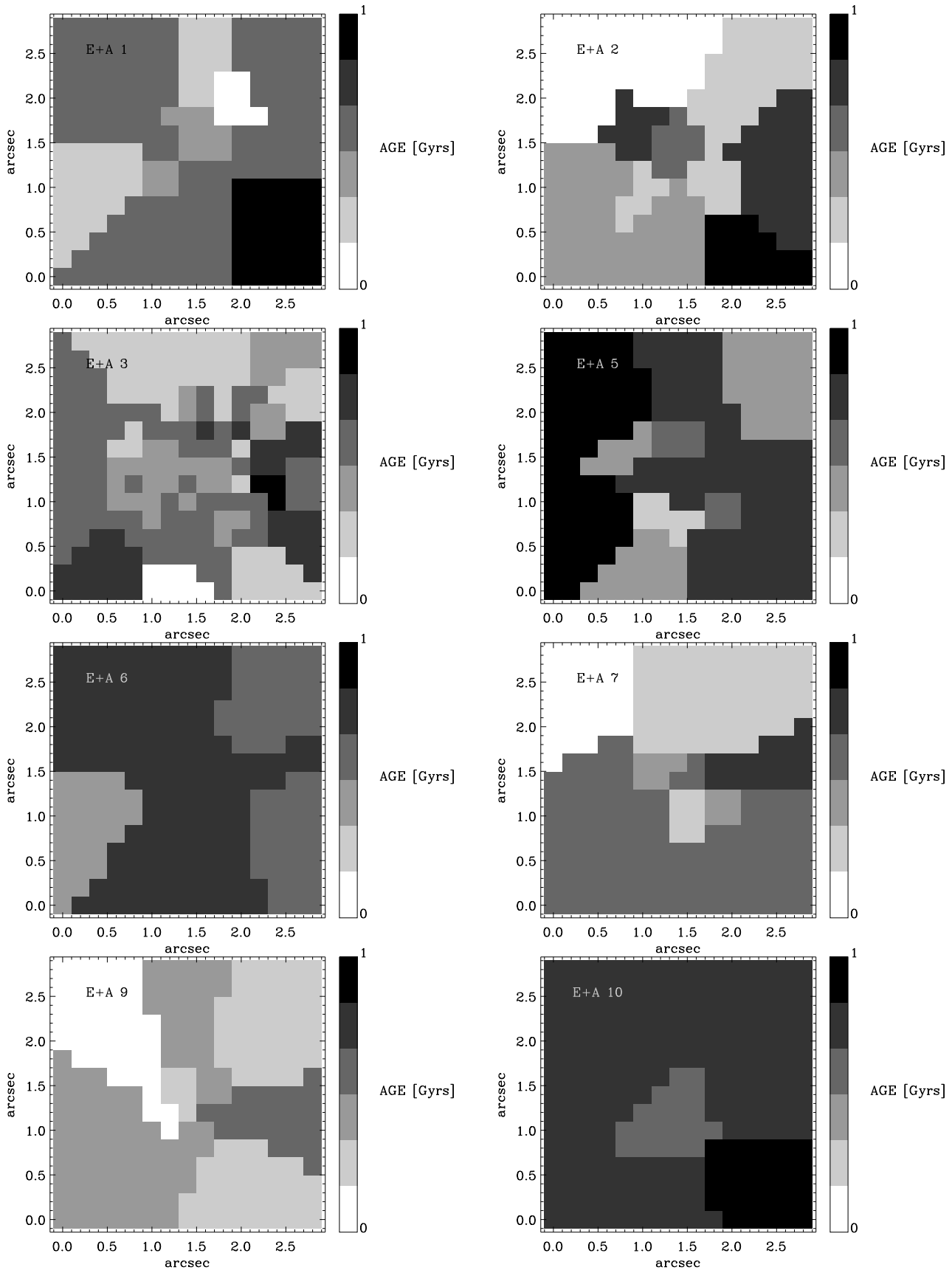


Figure 10. 'Age' maps constructed by taking the weighted average age of the best fitting composition of stellar population models for each spatial element.

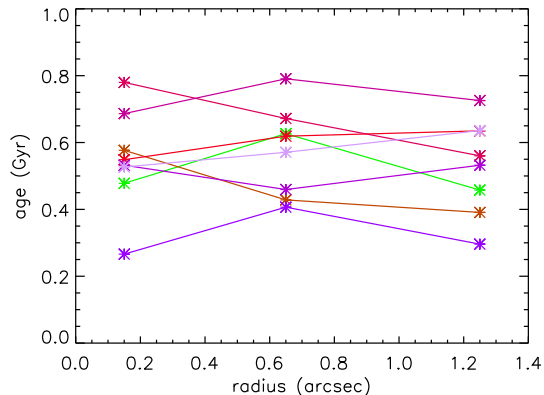


Figure 11. Age estimates versus radius measured from annular binning of the IFU data.

star-formation in a spiral disk is suddenly truncated then rotation should be present.

We have constructed two-dimensional velocity fields for each of the E+As in our sample that have IFU observations. The recession velocity for each spaxel is a free parameter in fitting the model templates, described in Section 4.8. The rotation fields are shown in Figure 12. In every case a clear rotation around the galaxy’s center is evident. The observed rotation velocities are generally of order $V \sin i \sim 60 \text{ km s}^{-1}$, although these are very much lower limits since the data only extend to radii of $\sim 1.5''$ (~ 2 to 5 kpc) and the rotation speed may continue to rise at larger radii. Also the data are smoothed by convolution with the seeing disk (and also binned spatially) which dampens the amplitude of the rotation (note: the statistical error on the velocity determination of each spaxel is generally $\sim 10 \text{ km s}^{-1}$). To further illustrate the ‘rotation curve’ behaviour seen across the face of the galaxies, the streaming velocities measured for each spaxel along the line that connects the maximum and minimum rotation velocities, are plotted in Figure 13. Here the *green stars* indicate the spaxels identified as having the maximum and minimum rotation velocities.

Although several spatially-resolved spectroscopic studies of E+A galaxies residing in clusters have reported strong rotation (Franx 1993; Caldwell et al. 1996), the only comprehensive study to date of the internal kinematics of nearby field E+A galaxies was performed by NGZZ. This study used long-slit spectroscopy to obtain spatially resolved spectroscopy of E+A galaxies from the Las Campanas Redshift Survey (Zabludoff et al. 1996). Of the NGZZ sample, 14 out of 20 show no evidence for rotation and two of the remaining 6 show only marginal evidence of rotation. Only 6 of 20 galaxies in the NGZZ sample have a rotational velocity of greater than $v_{\text{rot}} \sin i > 40 \text{ km s}^{-1}$ where the average galacto-centric radius of the measured velocity is $\sim 2.8 \text{ kpc}$ (converted to our assumed cosmology). However, NGZZ point out that the two galaxies with the most significant rotation are those that have the greatest radial coverage. In contrast, 6 out of 8 of the E+A galaxies studied here have $v_{\text{rot}} \sin i > 40 \text{ km s}^{-1}$, despite being measured over a similar physical radius. Moreover, the galaxies in our sample have a similar distribution in absolute magnitude and redshift to those in NGZZ’s sample. Typical large spiral galax-

ies measured at similar radii have $V_{\text{rot}} \sin i \sim 70\text{--}140 \text{ km s}^{-1}$ (Héraudeau et al. 1999); our sample is close to the lower end of this range with most of our E+A galaxies having rotation velocities of $\sim 60 \text{ km s}^{-1}$.

In Figure 14, we compare the kinematic properties of our sample to the NGZZ LCRS sample. In the top panel we show the measured $v_{\text{rot}} \sin i$ values for our sample (*black open squares*) along with the $v_{\text{rot}} \sin i$ values derived by NGZZ. We estimate $v_{\text{rot}} \sin i$ from the velocity maps in Figure 12 by selecting the spaxels which seem to correspond to the outermost part of the measured rotation curve. The NGZZ fitting technique simultaneously fitted for the kinematics of the young and old stellar populations and their results are plotted as the *blue diamonds* (young component) and the *red diamonds* (old component). In principle we should compare to the young component since our spectra are consistent with being ‘completely’ dominated by a young stellar population, although the two generally span the same parameter space. The rotation velocities measured from our sample overlap the high velocity end of NGZZ’s distribution, with most of the galaxies in their sample having significantly lower velocities. In the middle panel of Figure 14, we compare the central velocity dispersions, which were measured over the central $1''$ (*black squares*), to those measured by NGZZ (*red and blue diamonds*). The distribution of central velocity dispersions are similar in the two samples. Also shown are the velocity dispersions of normal early-type systems (*small black points*) from Faber et al. (1989) where we have converted their *B*-band magnitudes to *R*-band values assuming $B - R = 1.25$ (NGZZ). Both our data and that of NGZZ are too bright to be on the normal early-type relation. However, model predictions of the expected dimming of E+A galaxies as they evolve suggest they should fade by 0.5–1 mag over the subsequent 1–2 Gyrs (NGZZ; Poggianti et al. 1999; Kelson et al. 2000). The *green squares* in Figure 14 show where our E+A galaxies would lie once they had faded by this (1.0 mag) amount, and we see they now overlap the early-type relation.

In the bottom panel of Figure 14 we compare the $v_{\text{rot}} \sin i / \sigma$ values for the two samples. Naturally since our sample has larger rotation velocities but similar velocity dispersions the $v_{\text{rot}} \sin i / \sigma$ distribution of our sample corresponds to the high end of the $v \sin i / \sigma$ distribution from NGZZ.

A method for quantifying the rotation of galaxies specifically designed for use with two dimensional IFU data was developed by Emsellem et al. (2007). Their parameter, λ_R , involves luminosity-weighted averages over the two dimensional kinematic field provided by IFU data and acts as a proxy to the observed projected stellar angular momentum per unit mass. Using this parameter, Emsellem et al. (2007) are able to clearly separate the elliptical galaxy population into two distinct subsets, the ‘fast rotators’ which tend to be relatively low luminosity galaxies ($M_B > -20.5$), and ‘slow rotators’ which span the entire range in luminosity. Emsellem et al. (2007) found three quarters of the SAURON sample to be fast rotators. In Figure 15 we show the values of λ_R measured for the 8 E+A galaxies in our sample for which we have IFU observations. In the top panel we show the λ_R parameter measured for each E+A galaxy versus the radius over which it was measured, and in the bottom panel we plot λ_R against galaxy ellipticity measured at twice the

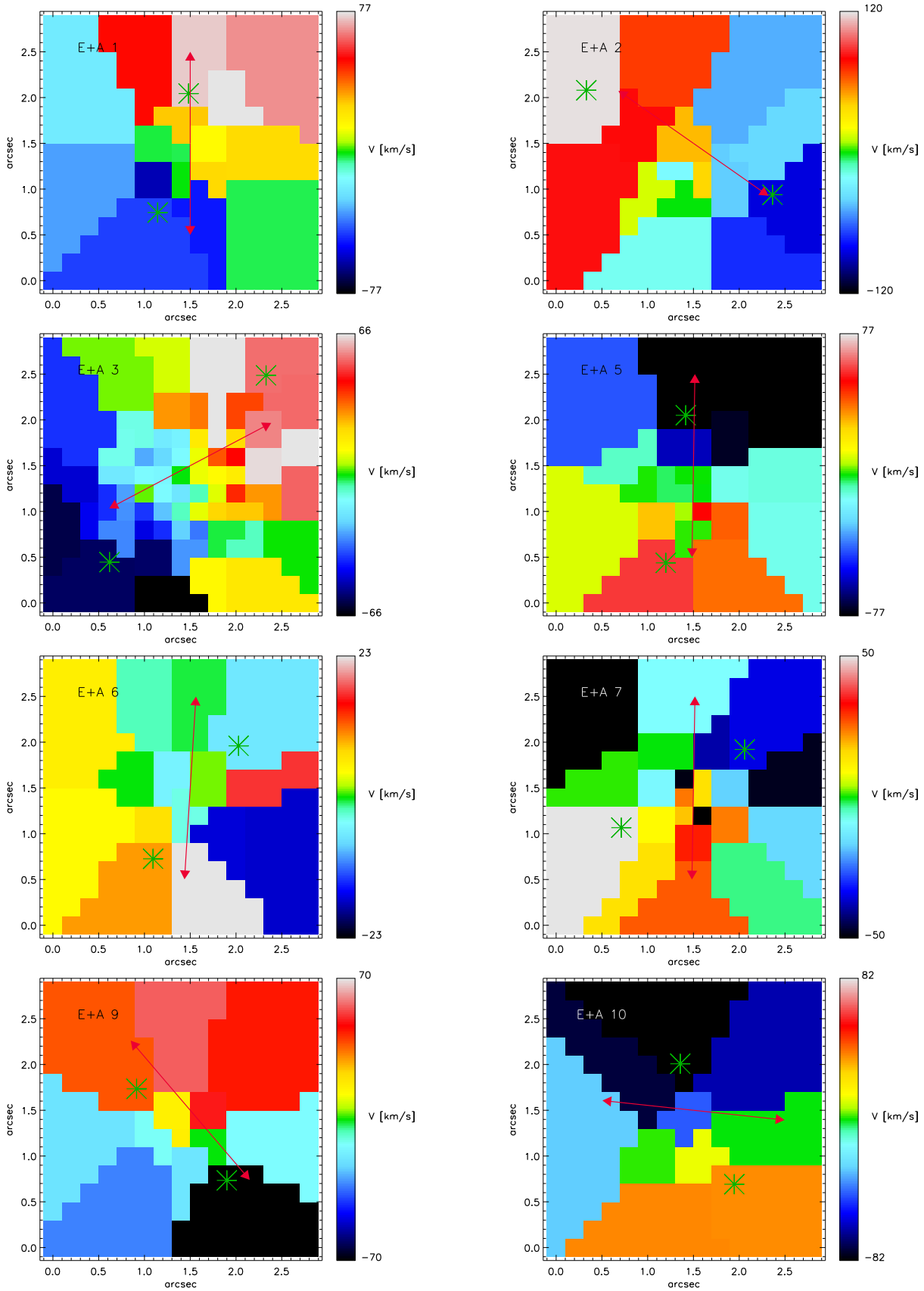


Figure 12. Two dimensional streaming velocity maps for our E+A sample. Rotation is clearly present in all cases. The green points mark the spaxels used to determine the maximum rotation velocity. The red arrows show the angle of the semi-major axes derived from the imaging.

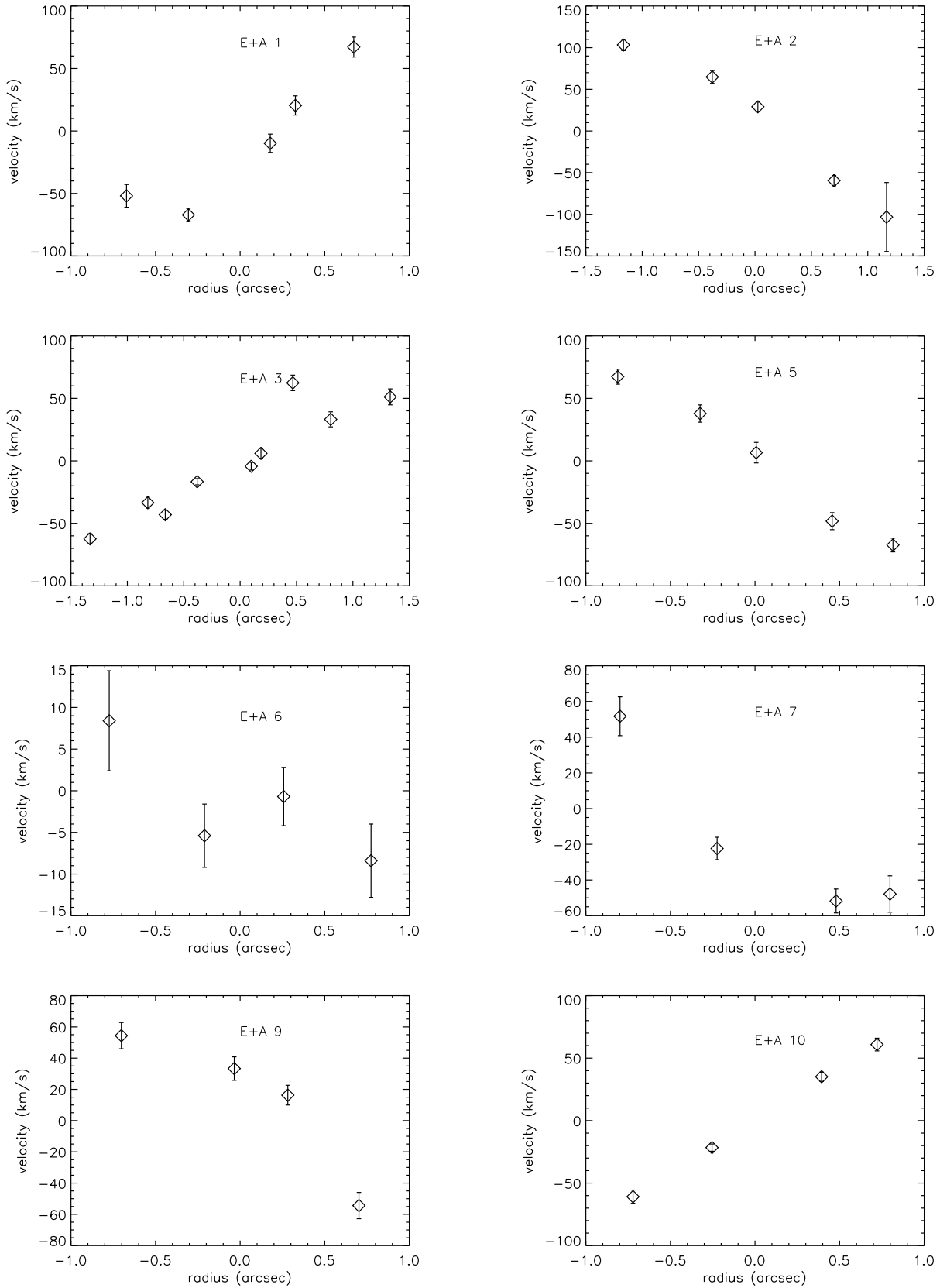


Figure 13. One dimensional rotation curve for our E+A sample. Rotation is clearly present in all cases.

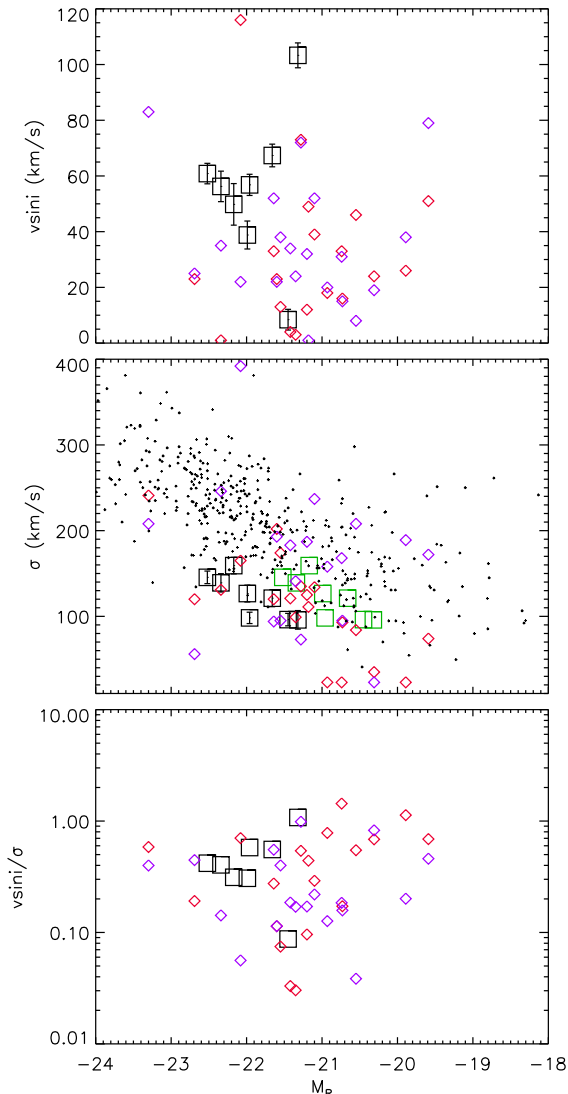


Figure 14. *Top panel:* The projected rotation velocities of our sample (black squares) compared to the sample of NGZZ (blue and red diamonds). Note the NGZZ fitting technique simultaneously fit for the kinematics of the young and old stellar populations and their results are plotted as blue diamonds (young component) and red diamonds (old component). *Middle panel:* Comparison of the central velocity dispersion of the NGZZ sample (blue and red diamonds) and our sample black squares. The small black points represent the Faber-Jackson of normal ellipticals and the green squares are our data dimmed by 1 mags which is the expected brightening due to the A-star light. *bottom panel:* comparison of $v \sin i / \sigma$ of the samples.

effective radius. In both plots we overlay the fast rotators (blue symbols and tracks) and the slow rotators (red symbols and tracks) from the SAURON sample. Comparison of the λ_R values found for our E+A galaxies with the tracks for the SAURON sample shows that 7 out of 8 of the E+As are consistent with being fast rotators and 1 out of 8, E+A_6, sits on the slow rotator tracks. We note, without implication, that E+A_6 is also the sole blue core object in our sample. E+A_2 has a large λ_R value in comparison to the

other galaxies in the sample and is also the galaxy which showed the strongest evidence of a substantial disk (see Figures 1 and 2). The other galaxies classified as fast rotators have λ_R values at the lower end of the fast rotator range.

There is some minimum value below which λ_R cannot be reliably measured (Emsellem et al. 2007) since noise in the data will always lead to some non-zero value of λ_R even for an object with zero true rotation. We can estimate whether or not we are detecting reliable values or λ_R by simulating this effect. We produced 10,000 simulated velocity fields for each of our objects by setting the velocity field in the IFU data to zero and adding in a random velocity to each spaxel based on the noise estimates. The values of λ_R produced in this manner were, on average, between 10 and 20 per cent of the values measured from the real data, being as small as 2 per cent for the high signal-to-noise data obtained for E+A_3 and as high as 53 per cent for the slow rotator E+A_6. This clearly demonstrates that we can reliably measure non-zero λ_R values. Emsellem et al. (2007) also found that the fast rotator population have well aligned photometric and kinematic axes. In Figure 12 we overplot as red arrows the position angle of the semi-major axes measured from the imaging. In most cases the photometric axis and kinematic axis are closely aligned although there are several exceptions. The accuracy of such a comparison is somewhat limited given the generally low ellipticities of our sample galaxies and the large spaxel size in the velocity data.

5 DISCUSSION

Our combined photometric and spectroscopic study of our E+A sample has allowed us to compile a wealth of information on their detailed structure and morphology and the internal colour distribution and kinematics of their recently formed population of young stars, which is spatially resolved on scales of 1-2 kpc. The primary motivation for acquiring and assembling these data is to significantly progress our understanding of the physical mechanisms responsible for E+A formation and their subsequent rapid spectral evolution. As we now discuss, our study has two important contributions to make in this context: (i) to much more firmly establish the key structural and kinematical properties of E+A galaxies, in particular those that provide the strongest clues as to their formation and evolution, and (ii) to cast new light on how E+A galaxies fit within the broader picture of general galaxy formation and evolution.

A key result to emerge from our study is a very clear picture as to the structural morphology and generic family of objects E+A galaxies generally belong to. The overall surface brightness profiles in Figure 2 show that they are consistent with being early-type systems with $r^{-1/4}$ -like profiles, with only one galaxy showing clear evidence for the presence of an exponential disk. This is further underscored by their visually-determined morphologies (which all lie in the narrow range S0-Sa; column 2 of Table 3), and their distribution within the central velocity dispersion versus magnitude plane (Figure 14), which is seen to be consistent with the Faber-Jackson relation after taking into account their higher transient luminosity resulting from the young A-star population. Both of these findings further corroborate the

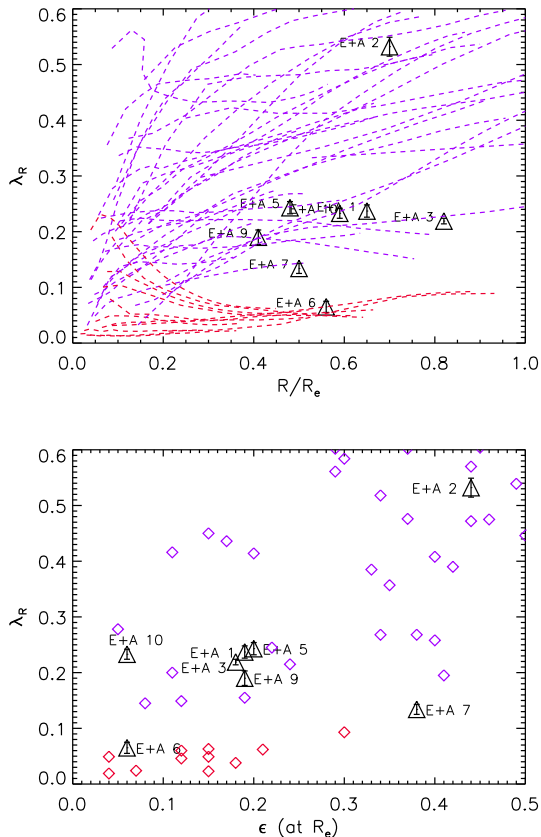


Figure 15. *Top panel:* The λ_R parameter from Emsellem et al. (2007) plotted against the radius at which it is measured (in units of the effective radius) for our E+A sample (*black triangles*). The *blue dashed lines* are the tracks for the fast rotators in the SAURON sample (Emsellem et al. 2007) and the *red dashed lines* are the tracks for the slow rotators. Seven out of eight of our E+As occupy positions in this plane corresponding to fast rotators. E+A.6 is the exception lying on the slow rotator tracks. *Bottom panel:* The λ_R parameter plotted against ellipticity for our E+A sample (*black triangles*) where the λ_R has been computed over the entire IFU area (i.e. out to the radii shown in the *top panel*) and the ellipticity is calculated at $2R_e$. The diamonds show the SAURON sample measured at $1R_e$. The blue symbols are the fast rotators and the red symbols the slow rotators. Again, with the exception of E+A.6 our sample overlap the fast rotators. Note: the reason we compute the ellipticity at $2R_e$ rather than $1R_e$ is to negate the effect of seeing on the ellipticity.

previous results of Yang et al. (2004), Yamauchi & Goto (2005), NGZZ, and Yang et al. (2008) thereby making them now well established properties of E+A galaxies.

Another important and common morphological attribute is the high incidence of tidal tails/arms/bridges and/or disturbed appearance, indicative of tidal interactions and merging. Our deep imaging shows approximately two-thirds of our sample exhibit features of this kind. This adds strong support for the conclusions drawn in earlier studies (Zabludoff et al. 1996; Yang et al. 2004; Blake et al. 2004; Yang et al. 2008) that interaction and merger activity is rife amongst the E+A population.

While E+A galaxies appear to be relatively homogeneous in terms of their morphology – predominantly early–

type systems, with a large fraction involved in ongoing or recent mergers and interactions – the same cannot be said for their internal colour distributions. As highlighted in columns 5 and 6 of Table 3, they can have either red, blue or irregular coloured cores, and have negative, flat or positive colour gradients. Similarly diverse behaviour in the colour properties has already been reported by Yamauchi & Goto (2005) in a sample of 22 E+A galaxies from the catalogue of Goto (2005).

A further and related curiosity is the large number of galaxies in our sample that have red cores. This seems counter to the view that their recent starburst activity was clearly widespread throughout their central regions, based on the spatial distribution of the E+A spectral signature and hence the young stars that were formed (as shown by the $H\delta_A$ maps in Figure 8). One possible explanation is that we are seeing a centralized starburst that is dust obscured, which would result in strong absorption lines but redder colours. Here the model subtracted images of our galaxies (shown in column 2 of Figure 1) are of interest, in particular the residual features very close to their centres, perhaps indicating the presence of dust lanes and dust obscuration. However, the evidence is at best marginal, with no indication that such features preferentially occur in the galaxies with red cores. Another explanation might be that the strongest young star contribution is located just outside the core, resulting in bluer colours peripheral to the core. Unfortunately, the spatial coverage of our spectroscopy is insufficient to test this hypothesis. Our IFU spectroscopy reveals that the $H\delta$ absorption is uniformly strong over the central few kiloparsecs but is inadequate in spatial coverage to discern any radial gradients. There is limited examples of spatially-resolved spectroscopy of E+A galaxies in the literature but these have indicated a preference for $H\delta$ strength which is centrally concentrated (NGZZ; Goto et al. 2008) in field E+As. In the intermediate redshift cluster AC114, Pracy et al. (2005) found a dichotomy in $H\delta$ distributions with examples of central concentration and central deficit.

The last but perhaps most important piece of information provided by our study is that, kinematically, our E+A galaxies are very homogeneous in that their populations of recently formed stars in all cases show unambiguous and significant rotational motion. The only other study of the internal kinematics of local field E+A galaxies is that of NGZZ. These authors reported much lower levels of rotation than found in this work for galaxies that have similar absolute magnitude and velocity dispersions distributions (see Figure 14). Also the average radius over which the kinematical measurements were made is essentially the same in both studies (~ 2.8 kpc). These very different results could possibly be due to technical reasons rather than intrinsic differences between the galaxies targeted in the two studies. The main difference between the data sets is our use of 2-dimensional spectroscopy compared with the long-slit spectroscopy used by NGZZ. IFU spectroscopy has the advantage of not requiring prior knowledge of the axis of rotation and does not suffer from problems associated with the misalignment of the rotation axis and the slit. We note that in our sample the rotation and semi-major axis are generally well aligned but in a subset of objects the differences in positional angle between the two can be substantial. We also note that strong rotation has been found to be prevalent in E+As in

the cluster environment (Franx 1993; Caldwell et al. 1996) and NGZZ point out that their study is at odds with those previous studies, although selection effects made it difficult to draw a firm conclusion in this regard.

While this ubiquitous rotation seen in our E+A sample is, in itself, a key result of this study, the strong evidence this provides that E+A galaxies are completely consistent with the ‘fast rotator’ population of early-type galaxies (as shown in the previous section), is a completely new and hitherto unrecognised connection. Importantly, this suggests that E+A galaxies may well be one progenitor population of the fast rotator galaxies, and hence a feeder population for producing galaxies of this type². Furthermore, there has already been considerable speculation in the literature as to the physical mechanism(s) responsible for the formation of the fast rotator population, which may well be applicable to E+A galaxies. Of most relevance here is the work of the SAURON team (Emsellem et al. 2007), who point out that the angular momentum in the inner parts of the fast rotators requires either gas-rich mergers and the absence of a major dry merger, which would expel angular momentum, or the building of a disk-like system via gas accretion. They argue that the specific angular momentum of fast rotators is mostly built up by either gas-rich minor mergers or other inflow of external gas. Very recent simulations by Bournaud et al. (2008), which have involved significant improvements in model resolution, suggest that major (as well as minor) mergers may in some situations produce fast rotator galaxies, with a significant amount of angular momentum being retained contrary to previous expectations. The dearth of slow rotators in our E+A sample may simply reflect the rarity of equal mass galaxy mergers.

The high incidence of the morphological signatures associated with tidal interactions and merging amongst our E+A galaxies provides a very direct pointer to this being a dominant formation mechanism in their case. Very detailed modeling of the expected structural, kinematical and spectrophotometric properties of an E+A galaxy produced in such an event has been published by Bekki et al. (2005). This was in the specific case of the merger of two gas-rich spirals, whose relative masses were varied to simulate both major and minor mergers. These simulations clearly demonstrated that a spheroid-dominated system is formed, which has a positive radial colour gradient and a negative radial H δ absorption strength gradient. They also showed that the projected kinematical and spectroscopic properties of the simulated E+A galaxies can be remarkably different, depending on the orbital parameters of the merger, and the young stars formed in the merger should show more rapid rotation and a smaller central velocity dispersion than the underlying old stellar population. While some of these predictions are consistent with our observations (e.g., spheroidal morphology, strong rotation of the young stellar population), and some we cannot test (e.g., negative radial H δ gradient, kinematics of the old stellar population), the prediction of a positive colour gradient in the central regions is difficult to reconcile with the large fraction of red cores seen in our sample.

² Although, again, we caution that our observations only constrain the young stellar population which will make only a small contribution to the overall light at later times (> 1 Gyr).

While such simulation-based models are impressive in their level of detail and continue to improve (e.g. Bournaud et al. 2008), some caution needs to be taken in using them to interpret the observations since they are rather limited in their parameter space coverage, in particular the type of merger explored. The simulations of Bekki et al. (2005) focus solely on the merger of two gas-rich spirals, and provide no information on what might happen in the merger of a gas-rich galaxy with a gas-poor galaxy, or if one or both of these galaxies were not spirals. One of us (K.B.) is currently undertaking a new set of simulations which examine E+A galaxy formation via the merger of an already gas-poor early-type galaxy and a very gas-rich companion. While the results from these are very preliminary, they do show considerable promise in perhaps addressing the issue of how red cores and hence negative colour gradients might be formed. In the case of a gas-poor/gas-rich *minor* merger, the strong starburst triggered by the merger does not occur in the centre of the E+A host, leaving its initial red core intact. Moreover, the starburst components come from the gas-rich companion which is destroyed during the merging process. The A-type stars formed in the burst are dispersed into the inner regions of the E+A host, giving rise to the strong central Balmer absorption that is seen in the observations. Undertaking a full and complete comparison of the structural, kinematical and spectrophotometric predictions of these new models with our observational data set will be an important next step in trying to shed further clues on the details of E+A galaxy formation.

6 CONCLUSION

We have obtained IFU spectroscopy and deep multi-colour imaging of a sample of 10 nearby E+A galaxies and used them to investigate the spatial distribution of colours, absorption line strengths, stellar populations and kinematics in these systems. Our main conclusions are as follows:

- Morphologically our E+A galaxies are consistent with being early-type systems based both on radial surface brightness profiles and visual morphological classification.
- Our deep imaging reveals a high rate of interactions and tidal features with 6 out of 10 galaxies displaying some evidence of disturbance. This is consistent with other morphological studies of E+As.
- The colour morphologies of our sample are diverse with most galaxies displaying a red core (relative to the outer parts of the galaxy) but with galaxies also having no core or irregular cores as well as a single galaxy with a distinct blue core. There is also a diversity in the large scale colour gradients of our sample. The integrated colours of the sample are blue as expected for E+A galaxies.
- The spatial distribution of A-star light mapped by H δ absorption or pseudo ‘age maps’ are uniform over the central few kiloparsec regions studied. But we are unable to spectroscopically probe the interesting region just beyond these radii where gradients are predicted by models.
- The young stellar populations in all the E+As in our sample show significant rotation which is inconsistent with the other major kinematic study of E+A galaxies by NGZZ despite similarity in the samples and radial extent probed.

- The kinematics of our sample are consistent with the overall population of early-type galaxies with 7 out of the 8 being classified as ‘fast rotators’ as defined by Emsellem et al. (2007).
- The high frequency of tidal disturbance and early-type morphologies of our sample argues against simple isolated truncation of a spiral disk. Our results are consistent with and suggestive of mergers and galaxy–galaxy interactions being a common formation mechanism for E+As.

7 ACKNOWLEDGEMENTS

This paper is based on observations obtained at the Gemini Observatory, which is operated by the Association of Universities for Research in Astronomy, Inc., under a cooperative agreement with the NSF on behalf of the Gemini partnership: the National Science Foundation (United States), the Science and Technology Facilities Council (United Kingdom), the National Research Council (Canada), CONICYT (Chile), the Australian Research Council (Australia), Ministério da Ciência e Tecnologia (Brazil) and SECYT (Argentina). We would like to thank the staff at the Gemini Observatory and the Australian Gemini Office for their expert assistance with our observations. This research was supported under the Australian Research Council’s Discovery Projects funding scheme (project number 0559688). We would like to thank the referee, Eric Emsellem, for careful and insightful comments which greatly improved this paper.

REFERENCES

- Abazajian K., Adelman-McCarthy J. K., Agüeros M. A., Allam S. S., Anderson K. S. J., Anderson S. F., Annis J., Bahcall N. A., Baldry I. K., Bastian S., and 143 coauthors, 2004, *AJ*, 128, 502
- Barnes J. E., Hernquist L. E., 1991, *ApJ*, 370, L65
- Bekki K., 1999, *ApJ*, 510, L15
- Bekki K., Couch W. J., Shioya Y., Vazdekis A., 2005, *MNRAS*, 359, 949
- Bekki K., Shioya Y., Couch W. J., 2001, *ApJ*, 547, L17
- Birnboim Y., Dekel A., 2003, *MNRAS*, 345, 349
- Blake C., Pracy M. B., Couch W. J., Bekki K., Lewis I., and 26 other authors 2004, *MNRAS*, 355, 713
- Bothun G. D., Dressler A., 1986, *ApJ*, 301, 57
- Bournaud F., Bois M., Emsellem E., Duc P. A., 2008, *Astron. Nachr.*, in press
- Caldwell N., Rose J. A., Franx M., Leonardi A. J., 1996, *AJ*, 111, 78
- Cappellari M., Copin Y., 2003, *MNRAS*, 342, 345
- Cappellari M., Emsellem E., 2004, *PASP*, 116, 138
- Colless M., Dalton G., Maddox S., Sutherland W., Norberg P., and 24 other authors 2001, *MNRAS*, 328, 1039
- Couch W. J., Sharples R. M., 1987, *MNRAS*, 229, 423
- Cross N. J. G., Driver S. P., Liske J., Lemon D. J., Peacock J. A., Cole S., Norberg P., Sutherland W. J., 2004, *MNRAS*, 349, 576
- Dekel A., Birnboim Y., 2006, *MNRAS*, 368, 2
- Dressler A., Gunn J. E., 1983, *ApJ*, 270, 7
- Eke V. R., Baugh C. M., Cole S., Frenk C. S., and 24 other authors 2004, *MNRAS*, 348, 866
- Emsellem E., Cappellari M., Krajnović D., van de Ven G., Bacon R., Bureau M., Davies R. L., de Zeeuw P. T., Falcón-Barroso J., Kuntschner H., McDermid R., Peletier R. F., Sarzi M., 2007, *MNRAS*, 379, 401
- Faber S. M., Wegner G., Burstein D., Davies R. L., Dressler A., Lynden-Bell D., Terlevich R. J., 1989, *ApJS*, 69, 763
- Franx M., 1993, *ApJ*, 407, L5
- Goto T., 2005, *MNRAS*, pp 53–+
- Goto T., Kawai A., Shimono A., Sugai H., Yagi M., Hattori T., 2008, *MNRAS*, 386, 1355
- Gunn J. E., Gott J. R. I., 1972, *ApJ*, 176, 1
- Héraudeau P., Simien F., Maubon G., Prugniel P., 1999, *A&AS*, 136, 509
- Hopkins P. F., Hernquist L., Cox T. J., Keres D., Wuyts S., 2009, *ApJ*, 691, 1424
- Kelson D. D., Illingworth G. D., van Dokkum P. G., Franx M., 2000, *ApJ*, 531, 184
- Kereš D., Katz N., Weinberg D. H., Davé R., 2005, *MNRAS*, 363, 2
- Kuntschner H., 2004, *A&A*, 426, 737
- Lewis I., Balogh M., De Propriis R., Couch W., Bower R., Offer A., Bland-Hawthorn J., Baldry I. K., Baugh C., Bridges T., Cannon R., Cole S., Colless M., and 20 other authors 2002, *MNRAS*, 334, 673
- Mihos J. C., Hernquist L., 1996, *ApJ*, 464, 641
- Mihos J. C., Richstone D. O., Bothun G. D., 1992, *ApJ*, 400, 153
- Moore B., Lake G., Katz N., 1998, *ApJ*, 495, 139
- Noguchi M., 1988, *A&A*, 203, 259
- Norris M. A., Sharples R. M., Kuntschner H., 2006, *MNRAS*, 367, 815
- Norton S. A., Gebhardt K., Zabludoff A. I., Zaritsky D., 2001, *ApJ*, 557, 150
- Poggianti B. M., Bridges T. J., Komiyama Y., Yagi M., Carter D., Mobasher B., Okamura S., Kashikawa N., 2004, *ApJ*, 601, 197
- Poggianti B. M., Smail I., Dressler A., Couch W. J., Barger A. J., Butcher H., Ellis R. S., Oemler A. J., 1999, *ApJ*, 518, 576
- Pracy M. B., Couch W. J., Blake C., Bekki K., Harrison C., Colless M., Kuntschner H., de Propriis R., 2005, *MNRAS*, 359, 1421
- Sánchez-Blázquez P., Peletier R. F., Jiménez-Vicente J., Cardiel N., Cenarro A. J., Falcón-Barroso J., Gorgas J., Selam S., Vazdekis A., 2006, *MNRAS*, 371, 703
- Semelin B., Combes F., 2005, *A&A*, 441, 55
- Shioya Y., Bekki K., Couch W. J., 2004, *ApJ*, 601, 654
- Smail I., Dressler A., Couch W. J., Ellis R. S., Oemler A. J., Butcher H., Sharples R. M., 1997, *ApJS*, 110, 213
- Swinbank A. M., Balogh M. L., Bower R. G., Hau G. K. T., Allington-Smith J. R., Nichol R. C., Miller C. J., 2005, *ApJ*, 622, 260
- Thomas D., Maraston C., Bender R., 2003, *MNRAS*, 339, 897
- Thomas D., Maraston C., Korn A., 2004, *MNRAS*, 351, L19
- Trager S. C., Worthey G., Faber S. M., Burstein D., Gonzalez J. J., 1998, *ApJS*, 116, 1
- Vazdekis A., Cardiel N., Cenarro A. J., Cervantes J. L., Falcón-Barroso J., Gorgas J., Jiménez-Vicente J., Martín-Hernández J. M., Peletier R. F., Sánchez-Blázquez P., Selam S. O., Toloba E., 2007, in Vazdekis A., Peletier R. F.,

- eds, IAU Symposium Vol. 241 of IAU Symposium, Stellar Population SEDs at 2.3 μ . pp 133–137
- Wild V., Peacock J. A., Lahav O., Conway E., Maddox S., Baldry I. K., Baugh C. M., Bland-Hawthorn J., Bridges T., and 20 other authors 2005, MNRAS, 356, 247
- Worthey G., Ottaviani D. L., 1997, ApJS, 111, 377
- Yamauchi C., Goto T., 2005, MNRAS, 359, 1557
- Yang Y., Zabludoff A. I., Zaritsky D., Lauer T. R., Mihos J. C., 2004, ApJ, 607, 258
- Yang Y., Zabludoff A. I., Zaritsky D., Mihos J. C., 2008, ApJ, 688, 945
- Zabludoff A. I., Zaritsky D., Lin H., Tucker D., Hashimoto Y., Shectman S. A., Oemler A., Kirshner R. P., 1996, ApJ, 466, 104